

CHALMERS
UNIVERSITY OF TECHNOLOGY

Axisymmetric perturbations and vertical displacement oscillatory modes driven by fast ions in tokamak plasmas

Downloaded from: https://research.chalmers.se, 2026-11-25 14:17 UTC

Citation for the original published paper (version of record):
Porcelli, F., Banerjee, D., Cavallero, S. et al (2027). Axisymmetric perturbations and vertical displacement oscillatory modes driven by fast ions in tokamak plasmas. Nuclear Fusion, 67(1). http://dx.doi.org/10.1088/1741-4326/aeb42f

N.B. When citing this work, cite the original published paper.

research.chalmers.se offers the possibility of retrieving research publications produced at Chalmers University of Technology. It covers all kind of research output: articles, dissertations, conference papers, reports etc. since 2004. research.chalmers.se is administrated and maintained by Chalmers Library

(article starts on next page)

nuclear fusion
IAEA

PAPER • OPEN ACCESS

Axisymmetric perturbations and vertical displacement oscillatory modes driven by fast ions in tokamak plasmas

To cite this article: F. Porcelli *et al* 2027 *Nucl. Fusion* **67** 016019

View the article online for updates and enhancements.

You may also like

- Regional ventilation imaging in normal and bronchoconstricted *in vivo* rabbit lungs using dynamic shuttle mode Xe-enhanced DECT imaging
Emma Verelst, Sam Bayat, Sylvia Verbanck et al.
- Time series regression network using exogenous variables for missing effective ion charge reconstruction in EAST tokamak
K. Jia, Z. Xu, Z.W. Wu et al.
- Collision of parallel vortex dipoles in a Bose–Einstein condensate
Guoquan Yang, Suying Zhang and Jingjing Jin

This content was downloaded from IP address 129.16.30.222 on 13/11/2026 at 08:34

OPEN ACCESS
IOP Publishing | International Atomic Energy Agency Nuclear Fusion
Nucl. Fusion **67** (2027) 016019 (19pp) https://doi.org/10.1088/1741-4326/aeb42f

Axisymmetric perturbations and vertical displacement oscillatory modes driven by fast ions in tokamak plasmas

F. Porcelli[1,2,*], D. Banerjee[1], S. Cavallero[1], T. Barberis[3], F. Qiu[2], A. Yolbarsop[2], L.-G. Eriksson[4] and C.C. Kim[5]

[1] Department of Applied Science and Technology, Polytechnic University of Turin, Torino, Italy
[2] Department of Plasma Physics and Fusion Engineering, University of Science and Technology of China, Hefei, China
[3] Princeton Plasma Physics Laboratory, Princeton, NJ, United States of America
[4] Department of Physics and Astronomy, Chalmers University of Technology, Gothenburg, Sweden
[5] SLS2 Consulting, San Diego, CA, United States of America

E-mail: francesco.porcelli@polito.it

Received 26 February 2026, revised 7 August 2026
Accepted for publication 14 October 2026
Published 30 October 2026

Abstract

Recent progress on the theory and numerical simulations of vertical displacement oscillatory modes (VDOM) in tokamak plasmas is reported. VDOM are driven unstable by energetic particles and can have an impact on plasma disruptions, plasma edge stability and confinement. These modes are a candidate, together with Global Alfvén Eigenmodes (GAE), to explain Alfvén-frequency $n = 0$ modes driven by fusion alpha particles recently observed on JET (Oliver *et al* 2026 *Phys. Rev. Lett.***136** 055101). Differences in the physical mechanisms underlying VDOM and GAE are discussed. An analytic dispersion relation that contains both VDOM and ideal-MHD unstable vertical displacements (VDs) is derived. Limits on plasma elongation for stable plasma operation against ideal-MHD VDs are discussed. While VDOM are generally immune against continuum damping, if the wall is brought very close to the plasma boundary and the plasma density remains relatively large up to the last-closed-flux-surface (as in the case of H-mode discharges), the VDOM oscillation frequency may interact with the Alfvén continuum spectrum, giving rise to continuum damping. Specific types of fast ion distribution functions that can provide an instability drive for $n = 0$ modes are considered. Numerical simulations of $n = 0$ modes obtained with the NIMROD code are shown, including a preliminary assessment of the fast ion instability drive for these modes.

Keywords: kinetic-MHD stability, axisymmetric modes, fusion alpha particles, tokamaks, vertical displacement oscillatory modes, energetic particles

(Some figures may appear in colour only in the online journal)

* Author to whom any correspondence should be addressed.

Original content from this work may be used under the terms of the Creative Commons Attribution 4.0 licence. Any further distribution of this work must maintain attribution to the author(s) and the title of the work, journal citation and DOI.

1. Introduction

A new type of fast ion driven instability involving axisymmetric modes (toroidal mode number $n = 0$) in magnetically confined tokamak plasmas was discovered recently [1]. The relevant mode has been dubbed vertical displacement oscillatory mode (VDOM). The linear dispersion relation for this mode was obtained analytically in [1–4]. An analytic estimate of the linear threshold for the destabilization of this mode in terms of critical fast ion density was discussed in [1]. VDOM oscillate with a relatively high frequency, of the order of the Alfvén frequency based on the poloidal magnetic field. High-frequency $n = 0$ modes have been observed in recent JET discharges, see e.g. Figure 3 of [5] and figure 12 of [6]. Alpha particle driven $n = 0$ modes have been clearly identified during the last DT3 campaign on JET [7, 8]. Axisymmetric $n = 0$ modes driven by Neutral Beam Injection (NBI) fast ions have also been observed on TCV [9] and on MAST-U [10]. The experimentally observed modes could be either Global Alfvén Eigenmodes (GAE) or VDOM [7, 8, 11], therefore, it is important to understand the difference between these two modes, both having toroidal mode number $n = 0$. Extrapolations and numerical simulations suggest that these modes are likely to be observed also in future tokamak experiments such as JT-60SA, SPARC, BEST, DTT, and ITER. Since both unstable VDOM and GAE rely on gradients of the fast ion distribution in velocity space, unstable $n = 0$ modes may lead to a faster relaxation of fusion alpha particles in velocity space, rather than alpha particle radial transport and loss of confinement. In this sense, unstable $n = 0$ modes should not pose a real danger to alpha particle confinement in fusion burning plasmas. Nevertheless, since $n = 0$ modes are global in nature and can affect the edge plasma region through the production of current sheets in the vicinity of magnetic X-points of the divertor separatrix [12], they may give rise to an important coupling between the plasma core, where the fast particle drive is normally dominant, and the plasma edge, with consequences for the stability of ELMs and an impact on the plasma dynamics in the divertor region. These considerations motivate further studies of $n = 0$ modes.

The main objective of this article is to review the recent progress in the understanding of VDOM. Nevertheless, the article also contains original work, namely: (i) A discussion (section 3) on the limits of plasma elongation for stable operation against the vertical instability in the ideal-MHD limit; (ii) An analytic study of VDOM in a straight tokamak configuration and in the circular cross section limit, aimed at clarifying conditions for which VDOM may be affected by continuum damping when the plasma-wall distance is reduced (section 4); (iii) Specific types of fast ion distributions giving rise to a positive drive for $n = 0$ modes, and an evaluation of the corresponding drive for $n = 0$ VDOM (section 6); (iv) New advances on the numerical simulation of $n = 0$ modes in realistic tokamak geometry using an initial-value code (NIMROD), with preliminary results showing VDOM driven by fast ions using a newly adapted kinetic-MHD module in NIMROD (section 7). Section 2 presents a short review of the analytic theory of VDOM. Section 5 discusses briefly the question of the impact of magnetic divertor X-points, where the equilibrium poloidal magnetic field vanishes, on $n = 0$ modes. Conclusions are presented in section 8. The appendix discusses the reason for a possible discrepancy between analytic results published in the early literature and more recent results reported here. This article is an extended version of an 8-page contributed paper presented at the last IAEA Fusion Energy Conference in Chengdu, China, 13–18 October 2025 [13].

2. A short review of the analytic theory of VDOM

There are four different types of $n = 0$ modes that are relevant for tokamak plasmas: (i) Geodesic Acoustic Modes (GAM) [14], which oscillate with a relatively low frequency of the order of the sound wave frequency; (ii) GAE [15]; (iii) VDOM [1, 2]; (iv) Zero-frequency Vertical Displacements (VD) [16] growing on the resistive wall time scale, which can be suppressed by an active feedback stabilization system. If left uncontrolled, the VD resistive wall mode can lead to VD Events (see, e.g. [17–19]) and disruptions. While the theory of GAM, GAE and VD is well developed, VDOM is a relatively new entry. For this reason, this article will be concerned mainly with the theory and numerical simulations of VDOM.

GAE and VDOM oscillate with a frequency of the order of the poloidal Alfvén frequency. They are both largely immune to continuum damping. Thus, they are both good candidates to explain the recent experimental observations of $n = 0$ modes mentioned in the Introduction. However, they have different mode structures, and the mechanisms underlying GAE and VDOM are also different.

According to the analysis of [15], the GAE can be defined as a shear-Alfvén internal mode, thus the main restoring force giving rise to plasma oscillations is related to field line bending. The GAE avoids continuum damping due to a minimum in the δ spectrum, so that its frequency lies just below the minimum value of $k_{||}v_{\rm A}$ reached inside the plasma. Consequently, the GAE mode structure tends to exhibit a rapid variation near the plasma edge, where the minimum of $k_{||}v_{\rm A}$ as function of radius normally is found, because the safety factor q and the plasma density tend to vary quickly in that region. Thus, the GAE is sensitive to details of q and of plasma density, while its frequency, being an internal mode, is largely insensitive to the plasma-wall distance [15].

By contrast, the VDOM is an external mode. The main restoring force giving rise to oscillations is related to the interaction between the plasma current and currents induced on the nearby first wall, under conditions of passive wall stabilization of the ideal-MHD vertical instability. When these conditions are satisfied, i.e. if the wall is sufficiently close to the plasma edge relative to the plasma elongation (see section 3 below), the resulting electromagnetic force coupling the plasma current and the induced wall currents opposes further vertical movements (in the limit of a perfectly conducting wall), causing a global vertical oscillation of the entire plasma column [2].

For the reasons explained in the previous paragraph, VDOM and VD are intimately related. A dispersion relation that can treat both VDOM and VD was obtained analytically, e.g. in [2], based on the reduced ideal-MHD model (in the absence of fast ions) and on a simplified straight-tokamak equilibrium [20, 21] that assumes an elliptical plasma boundary, with a and b the minor and major semi-axes, and a constant q profile. The choice of a flat q profile was made to exclude *a priori* the possibility for the chosen equilibrium to support GAE modes, because with a flat q a minimum in the $k_{||}v_A$ spectrum cannot occur (unless unrealistic, non-monotonic plasma density profiles are assumed), therefore establishing the VDOM as a totally independent mode. A further hypothesis that greatly simplifies analytic work is to assume that the plasma is confined within a resistive wall that is also taken to be an ellipse with semi-axes a_w and b_w satisfying the plasma boundary-wall confocality condition: ${b_w}^2-{a_w}^2=b^2-a^2$. We observe that confocality was also used in the pioneering work by Laval *et al* [22], although only an energy-principle analysis in the presence of a perfectly conducting wall, but no normal mode analysis, was carried out in that work. In this connection, we would like to mention the interesting article by Chukashev and Pustovitov [23], where analytic estimates of the VD growth rate were obtained for an elliptical plasma and for a resistive wall with circular cross section using a Green's function method.

The above assumptions on the plasma/wall geometry and idealized equilibrium profiles are formulated to obtain analytic solutions that elucidate the mechanisms and structures underlying the $n=0$ modes of interest and provide a benchmark for numerical simulations. However, these analytic solutions can at most suggest a qualitative interpretation of the $n=0$ oscillations observed in tokamak experiments. For a more detailed comparison with experiments, numerical work becomes necessary. We refer the reader to section 7 of this article for a discussion of how VDOMs were recognized in numerical simulations with realistic tokamak geometry and plasma equilibrium profiles.

The dispersion relation for $n=0$ modes that treats on equal footing VDOM and VD, with a resistive wall, is cubic for the complex eigenfrequency $\gamma=-i\omega$, see equation (1) here below. One of the early articles where the cubic dispersion relation first appeared was by Wesson [24], based on the same analytic simplifications listed above, i.e. straight tokamak equilibrium with uniform current density, elliptical plasma boundary and confocal elliptical wall, which are the same simplifying assumptions used by Laval *et al* [22]. This cubic dispersion relation was rederived in [2, 3], but although the derivation in [2, 3] used exactly the same assumptions as those made by Wesson, an important difference in the geometrical wall parameter D appearing below was found. This difference is highlighted at the end of section 3 and a possible explanation for this discrepancy is discussed in the appendix.

The cubic dispersion relation derived in [2, 3] reads as follows:

$$\gamma^3+\frac{\gamma^2}{(1-\hat{e}_0D)\,\tau_\eta}+\gamma\omega_0^2+\frac{\omega_0^2}{(1-D)\,\tau_\eta}=0 \qquad (1)$$

where τ_η is the resistive wall time, $e_0=(b^2-a^2)/(b^2+a^2)$ is the ellipticity parameter, $\hat{e}_0=\kappa e_0/(1+\kappa)$, $\kappa=b/a>1$ is the plasma elongation, $D=D(\kappa,b/b_w)$ is a geometric wall parameter defined in equation (4) (see section 3 below),

$$\omega_0=\left(\frac{D-1}{1-\hat{e}_0D}\right)^{1/2}\gamma_\infty,\ \text{where}\ \gamma_\infty=\frac{2\kappa}{1+\kappa^2}\left(\frac{\kappa-1}{\kappa}\right)^{1/2}\tau_A^{-1},$$
$$\text{and}\ \tau_A=\frac{B_p'}{(4\pi\,\varrho_m)^{1/2}}. \qquad (2)$$

In this dispersion relation, τ_A is the poloidal Alfvén time and γ_∞ is the ideal-MHD VD growth rate found in the no-wall limit, $b/b_w\to 0$, where also $D\to 0$ (see section 3). The roots of interest for our discussion are those corresponding to the two solutions $\omega=\pm\omega_0$ found in the limit of a perfectly conducting wall, $\tau_\eta\to\infty$. When $D<1$, ω_0^2 is negative and one of the two roots corresponds to an ideal-MHD unstable VDs, growing on the Alfvén time scale, i.e. a few micro-seconds for typical tokamak parameters (e.g. plasma density $n\sim 10^{20}m^{-3}$, magnetic field $B\sim 1T$, $a\sim 1\ m$). It would be impossible to prevent the rapid growth of a VDE in that limit. Passive-wall stabilization of rapidly growing VDs requires $D>1$. When this inequality is satisfied, ω_0^2 is a real positive quantity and the two solutions of interest are oscillatory in the ideal-wall limit. These two oscillatory solutions are what we refer to as VDOM. We point out that the dispersion relation (1) does not contain $n=0$ GAE, because of the assumption of a constant equilibrium current density (this assumption is relaxed in numerical work, see section 7). Also, it does not contain $n=0$ GAM oscillating at the sound frequency, which are caused by finite-β effects ($\beta=$ plasma pressure/magnetic pressure) outside the scope of the present article.

Thus, stable tokamak operation requires values of $D\geqslant 1$, i.e. passive wall stabilization. When dealing with VDOM, we will assume that the criterion $D\geqslant 1$ is always satisfied. When a resistive wall is considered, and for values of D not very close to unity such that $\omega_0\sim\tau_A^{-1}$, the relevant regime is $\omega_0\tau_\eta>>1$. In that limit, the three roots of dispersion relation (1) are

$$\omega=\pm\omega_0-\mathrm{i}\frac{(1-\hat{e}_0)\,D}{2\,(D-1)\,(1-\hat{e}_0D)\,\tau_\eta};\ \gamma=\frac{1}{(D-1)\,\tau_\eta}. \qquad (3)$$

The first two roots in equation (3) correspond to VDOM oscillating with a frequency $\Re(\omega)=\pm\omega_0$ ($\Re$ stands for 'real part'). As we can see, VDOMs are stable normal modes with a damping rate related to the wall resistivity. However, VDOMs can be driven unstable by fast particles [1], as discussed in sections 6 and 7.

The third, zero-frequency root shown in equation (3) corresponds to a $n=0$ VD slowly growing on the resistive wall time scale, i.e. a few milliseconds for typical tokamak parameters. Since in this regime the VD grows slowly, it can be completely suppressed by active feedback stabilization. We observe, however, that close to ideal-MHD marginal stability, i.e. when D is close to unity and the condition $\omega_0\tau_\eta>>1$ is not satisfied, the resistive VD can grow much more rapidly, with a growth rate scaling with a fractional power (smaller than unity) of wall resistivity. This regime was discussed, e.g. in [4, 25] and in the

PhD thesis by Yanovskiy [26] (see also other references cited in that thesis). Thus, close to ideal-MHD marginal stability, the active feedback stabilization systems that normally operate in present-day tokamak experiments may not be capable of preventing the growth of a VD resistive wall mode because of its rapid growth rate, and a VD Event becomes more difficult to avoid.

Finally, we point out that the existence of oscillatory solutions of the cubic dispersion relation for $n = 0$ modes, slightly damped by wall resistivity, was also noted by other authors, see, e.g. [27–29]. Also, there are articles where toroidicity effects in analytic estimates of the VD growth rate are included. One such pioneering article is Fukuyama *et al*, see [30]. However, in that article, as well as in [27–29], the emphasis was on the growth and control of the usual, non-rotating VD resistive wall mode, while the VDOM and its related physics went unnoticed. In fact, the importance of VDOMs stems from their Alfvénic character, causing VDOM to be driven unstable by the resonant interaction with energetic particles in a tokamak plasma, as was found in [1] and further discussed in sections 6 and 7 of this article.

3. How much elongation is too much elongation?

Let us discuss in more detail the criterion $D \geqslant 1$ for the stabilization of the ideal-MHD VD and the consequent occurrence of VDOM. For the analytic model introduced in [2–4] (see also [22]), the expression for the geometric wall parameter is

$$D\left(\kappa, b/b_{\rm w}\right) = \frac{\kappa^2+1}{\left(\kappa-1\right)^2}\left\{1-\left[1-\frac{\kappa^2-1}{\kappa^2}\left(\frac{b}{b_{\rm w}}\right)^2\right]^{1/2}\right\}. \tag{4}$$

As pointed out in section 2, this expression assumes confocal ellipses for the plasma boundary and the plasma wall, and the equilibrium is up-down symmetric. It is, therefore, a rather crude approximation of the actual tokamak equilibrium configuration. X-points in a double-null configuration, lying on a divertor separatrix, are implied by this approximation [20]. However, the hot plasma is assumed to extend to an elliptical boundary and not to the magnetic separatrix, so that the X-points lie either in vacuum or in a cold, halo plasma region (we shall discuss in section 5 the consequences of relaxing this assumption). In a real tokamak experiment, the equilibrium may not be up-down symmetric and plasma shaping normally includes triangularity, a potentially important effect neglected in the present analysis. Furthermore, plasma-facing components are often placed inside the vacuum chamber to ensure passive wall stabilization of the ideal-MHD vertical instability. Bearing in mind all these caveats, we may use equation (4) to discuss a very relevant question: are there limits on plasma elongation for stable plasma operation against the onset of ideal-MHD VDs?

The short answer to this question is: no, in principle there are no limits on plasma elongation, if the wall can be placed sufficiently close to the plasma boundary. This is illustrated by figure 1, where we set $D\left(\kappa_{\rm crit}, b/b_{\rm w}\right) = 1$ and we solve for $\kappa_{\rm crit}$ as function of $b/b_{\rm w}$. As one can see from this figure, $\kappa_{\rm crit} \to \infty$ when the plasma touches the wall, $b/b_{\rm w} = 1$. However, in practice some distance must always be allowed between the plasma and the wall. Therefore, in practical terms, a critical elongation does exist. In figure 2, we show D as function of κ for different values of $b/b_{\rm w}$. The stable domain corresponds to values of $D > 1$. One can see that for values of $b/b_{\rm w}$ between 0.7 and 0.9, the critical elongation can vary significantly, from $\kappa_{\rm crit} = 2$ to $\kappa_{\rm crit} = 3.7$. At small values of, a simple calculation shows that

$$\kappa_{\rm crit} \approx 1 + 2\left(\frac{b}{b_{\rm w}}\right)^2 \text{ for } \frac{b}{b_{\rm w}} << 1$$

As discussed in [4], another important consequence of confocality between the elliptical plasma boundary and the elliptical wall is that the marginal stability condition, $D = 1$, corresponds to the situation where the wall intercepts the X-points (as was also found by Laval *et al* [22]). Ideal-MHD stability of VDs requires the X-points to lie outside the vacuum chamber. When comparing with realistic tokamak equilibria, this criterion appears to be somewhat restrictive, as for a given value of $b/b_{\rm w}$ the actual wall in a tokamak experiment is closer on average to the plasma than the confocal wall assumed in the cited analytic work. Furthermore, single-null divertor configurations normally have one magnetic X-point inside the vacuum chamber and a second one outside. Thus, numerical

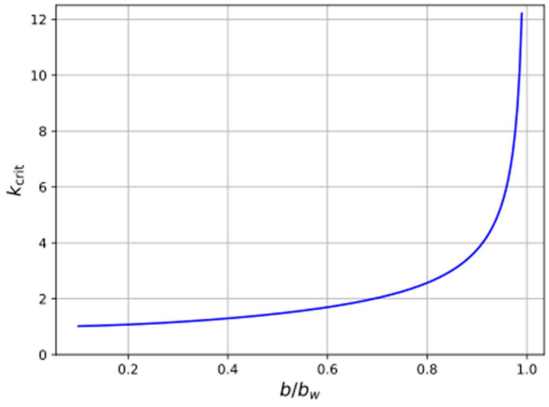

Figure 1. Critical elongation, $\kappa_{\rm crit}$, vs normalized plasma-wall distance, $b/b_{\rm w}$. When the plasma touches the wall, $b/b_{\rm w} = 1$.

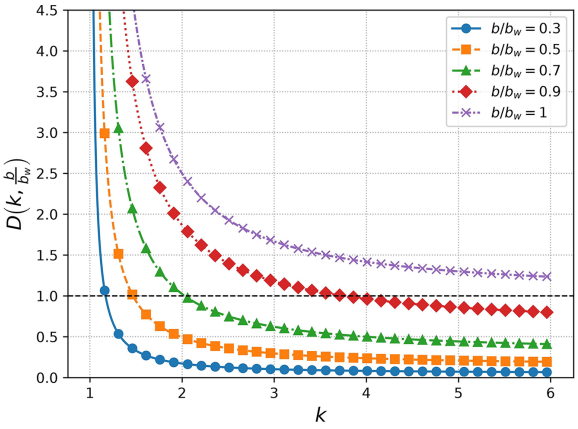

Figure 2. The geometric wall parameter, $D\left(\kappa, b/b_{\rm w}\right)$, vs elongation, κ, for different values of the normalized plasma-wall distance, $b/b_{\rm w}$.

work with more accurate plasma equilibria and wall geometry is required. However, it appears from this analysis that, for a double-null divertor configuration where both magnetic X-points lie inside the vacuum chamber, and considering the actual wall geometry, the ideal-MHD stability criterion can at best only marginally be satisfied, which motivates the use of plasma-facing coils inside the vacuum chamber to help guarantee passive wall stabilization.

The idealized equilibrium [20, 21] used in [2–4] and in this article, leading to equation (4) for the geometric wall parameter D and to the criterion $D\geqslant 1$ for ideal-MHD stability of VD, is the same equilibrium used in the pioneering work by Laval *et al* [22]. If expressed in terms of κ and $\kappa_{\rm w}=b_{\rm w}/a_{\rm w}$, and keeping in mind the confocality condition, ${b_{\rm w}}^2-{a_{\rm w}}^2={b}^2-{a}^2$, the criterion $D\geqslant 1$ becomes

$$D=\frac{\kappa^2+1}{(\kappa-1)^2}\frac{\kappa_{\rm w}-1}{\kappa_{\rm w}}\geqslant 1 \tag{5}$$

which is consistent with [22], but corrects a suspected misprint in [24], also appearing in the widely used book *Tokamaks*, by Wesson, see the expression for D given at the end of section 6.15 of [31]. For a more detailed comparison between our expression for the geometric wall parameter D and Wesson's, we refer the reader to the appendix. Also, the appendix contains a short discussion on how, in some cases (especially when triangular shaping is not very strong), the analytic results that assume an idealized, elliptical wall confocal to an elliptical plasma boundary may be used to provide upper and lower bounds on the ideal-MHD stability of VDs and the possible interval of values for the VDOM oscillation frequency in actual tokamak experiments.

4. The circular cross-section limit

At small elongation, $\kappa-1<<1$, the geometric wall parameter is well approximated by

$$D\approx\frac{2}{\kappa-1}\left(\frac{b}{b_{\rm w}}\right)^2. \tag{6}$$

Thus, for κ approaching unity, and keeping the wall at a finite distance from the plasma boundary, the parameter D diverges. This corresponds to the limit where a cylindrical plasma column with a circular cross section of radius $a=b$ is bound by a perfectly conducting wall with concentric cross section of radius $a_{\rm w}=b_{\rm w}>a$. We observe that also in this limit an oscillatory mode persists. Referring to the expression for ω_0 given in equation (2), noting that in the limit $\kappa\to 1$, $\widehat{e}_0 D\to (b/b_{\rm w})^2$ and $\gamma_\infty^2\approx(\kappa-1)\,\tau_{\rm A}^{-2}$, and assuming that also $\kappa-1<2(b/b_{\rm w})^2$ (which maintains D above unity), we find

$$\omega_{0c}^2=\frac{2(b/b_{\rm w})^2}{1-(b/b_{\rm w})^2}\tau_{\rm A}^{-2} \tag{7}$$

where the subscript 'c' has been introduced to denote the VDOM oscillation frequency in the circular limit. The nature of this oscillation should be clear. In the limit $b/b_{\rm w}\to 0$, where the wall is at infinity, $\omega_{0c}\to 0$ and a rigid displacement of the plasma column along any direction orthogonal to the cylinder axis is neutrally stable as no restoring force is present. However, if a perfectly conducting wall is present at a finite distance, as soon as the plasma column is displaced, currents are induced at the wall; the interaction between the plasma current and the induced wall currents gives rise to a restoring force and hence to an oscillation of the plasma column. As a matter of fact, using the qualifier 'vertical' in VDOM would be a misnomer in the circular cross section limit, because all directions orthogonal to the cylinder axis are equivalent in this case. Nonetheless, as soon as non-zero values of $\kappa-1$ are considered, this degeneracy is broken, and we can consider a 'vertical' direction (along the elliptical plasma and wall major axes) and a 'horizontal' direction (see [32]). Besides, there is a more compelling reason why it makes sense to preserve the terminology 'vertical' also in the circular limit: if one thinks of a 'straight tokamak' with circular cross section as approximating a toroidal plasma in the limit of very large aspect ratio R_0/a, then it is natural to think of a *vertical* shift of the plasma column as being a shift in the direction orthogonal to the equatorial plane of the equivalent torus. By contrast, a *horizontal* shift would be along the torus inboard-outboard direction. Then, one can see that a rigid shift of the 'straight tokamak' corresponding to an axisymmetric mode could occur only in the vertical direction, while a rigid horizontal shift would necessarily correspond to a mode with toroidal mode number $n=1$.

The VDOM dispersion relation in the circular cross section limit, yielding the oscillation frequency (7), was studied in [32]. It is useful to revisit the derivation of the dispersion relation starting from a cylindrical plasma with circular cross section, because in [32] not enough attention was given to the fact that the mode frequency, as given by equation (7), can exceed the Alfvén frequency when the wall is brought close to the plasma boundary. For the special, idealized equilibrium considered in [32] and also here, see equation (13) below, $\omega_{0c}\tau_{\rm A}$ becomes larger than unity when $a_{\rm w}<\sqrt{3}a$ (we adopt the more standard notation $a_{\rm w}=b_{\rm w}$ for the radius of the circular wall cross-section and $a=b$ for the plasma minor radius in the circular limit). Values of $\omega_{0c}\tau_{\rm A}\geqslant 1$ can give rise to an interaction of the VDOM with the Alfvén continuum spectrum and therefore can be associated with continuum damping. However, we anticipate that continuum damping is not a general feature of VDOM. For different plasma density profiles, such as, for example, that indicated in equation (28) below, $\omega_{0c}\tau_{\rm A}$ remains below the minimum of $k_||v_A$ even when the wall is brought to the plasma edge, so that continuum damping never occurs.

The derivation of the normal mode equation for a cylindrical plasma with circular cross section based on the reduced ideal-MHD model is fairly standard and can be obtained, for instance, from [15] in the limit of a uniform equilibrium current density, or from [30] in the large aspect ratio limit. However, this derivation is briefly reported here for the reader's convenience, and to highlight the mathematical aspects associated with the possibility of continuum damping for VDOM. The starting point is the linearized version of the

standard, reduced-ideal-MHD model [32, 33] involving the flux function $\psi(r,\vartheta,t) = \psi_{eq}(r) + \tilde{\psi}(r,\vartheta,t)$ and the stream function $\tilde{\varphi}(r,\vartheta,t)$. Here, the subscript '*eq*' indicates equilibrium quantities and an over-tilde indicates small perturbations. In dimensionless form:

$$\frac{\partial\tilde{\psi}}{\partial t} + [\tilde{\varphi},\psi_{eq}] = 0 \tag{8}$$

$$\frac{\partial}{\partial t}\nabla\cdot(\varrho_{eq}\nabla\tilde{\varphi}) = \left[\tilde{\psi},J_{eq}\right] + \left[\psi_{eq},\tilde{J}\right]. \tag{9}$$

In these equations, square brackets are defined as in $[\chi,\psi] = e_z\cdot\nabla\chi\times\nabla\psi$, where '$z$' is the ignorable coordinate, e_z is the unit vector along the ignorable z-direction (the cylinder axis), and $J = \nabla^2\psi$ is the current density along the z-direction. Furthermore, $\varrho_{eq}(r)$ is the equilibrium mass density and $J_{eq}(r)$ is the equilibrium current density. Time and space are made dimensionless by normalizing to the Alfvén time, τ_A, and to the plasma minor radius, a. Thus, in dimensionless form, $r = 1$ is the normalized radius of the circular plasma boundary and we indicate with $r_w \geqslant 1$ the dimensionless wall radius. The mass density is normalized to its on-axis equilibrium value and the current density to twice its on-axis equilibrium value.

If we further assume that perturbed quantities vary as

$$\tilde{\psi}(r,\vartheta,t) = \hat{\psi}(r)\,e^{-i\omega t+i\vartheta} \tag{10}$$

and similar for $\tilde{\varphi}(r,\vartheta,t)$ and for $\tilde{J}(r,\vartheta,t)$, dropping the hats for simplicity of notation, and eliminating $\tilde{\varphi}$ from equations (8) and (9), we obtain the ordinary, second-order, homogeneous differential equation for the amplitude $\psi(r)$ of the perturbed flux

$$\omega^2\left\{\frac{\mathrm{d}}{\mathrm{d}r}\left[r\varrho_{eq}\frac{\mathrm{d}}{\mathrm{d}r}\left(\frac{r}{\psi'_{eq}}\psi\right)\right] - \frac{\varrho_{eq}}{\psi'_{eq}}\psi\right\} = \psi'_{eq}J - J'_{eq}\psi \tag{11}$$

where the amplitude of the perturbed current density is

$$J(r) = \frac{1}{r}\frac{\mathrm{d}}{\mathrm{d}r}\left(r\frac{\mathrm{d}\psi}{\mathrm{d}r}\right) - \frac{\psi}{r^2}. \tag{12}$$

A 'prime' in equation (11) indicates radial derivative of the related equilibrium field. We point out that the normal mode equation (11) is in agreement with equation (3) of [15] for $n = 0$ and $B_z = constant$. The normal mode equation (11) can also be obtained from equation (24) of [30] in the limit of an ideal walls and infinite aspect ratio.

To solve equation (11), we must choose equilibrium profiles for the mass density, the current density and the corresponding magnetic flux. Following [2, 22, 32], analytic work becomes very simple if we choose step functions for $\varrho_{eq}(r)$ and $J_{eq}(r)$,

$$\varrho_{eq}(r) = H(1-r) \quad \text{and} \quad J_{eq}(r) = 2H(1-r) \tag{13}$$

where $H(x)$ is the Heaviside step function. The corresponding equilibrium flux is

$$\psi_{eq}(r) = \frac{1}{2}r^2 \ \text{ for } r\leqslant 1 \ \text{ and } \ \psi_{eq}(r) = \frac{1}{2} + \ln(r) \ \text{ for } r\geqslant 1 \tag{14}$$

with $\psi_{eq}(r)$ continuous with its first derivative across $r = 1$. Then, for $0\leqslant r < 1$, $\varrho_{eq} = 1$, $\psi'_{eq}(r) = r$, $J'_{eq} = 0$; for $1 < r\leqslant r_w$, $\varrho_{eq} = J'_{eq} = 0$; equation (11) in the two intervals, denoted with superscript '$-$' for $0\leqslant r < 1$ and '$+$' for $1 < r\leqslant r_w$, reduces to

$$\left(\omega^2 - 1\right)\left[\frac{\mathrm{d}}{\mathrm{d}r}\left(r\frac{\mathrm{d}\psi^-}{\mathrm{d}r}\right) - \frac{\psi^-}{r}\right] = 0 \ \text{ for } 0\leqslant r < 1 \tag{15a}$$

and

$$\psi'_{eq}J = \frac{\mathrm{d}}{\mathrm{d}r}\left(r\frac{\mathrm{d}\psi^+}{\mathrm{d}r}\right) - \frac{\psi^+}{r} = 0 \ \text{ for } 1 < r\leqslant r_w. \tag{15b}$$

Thus, the solution that satisfies the boundary conditions $\psi^-(0) = 0$, $\psi^+(0) = 0$, and that is continuous across $r = 1$ is, apart from an arbitrary multiplicative constant

$$\psi^-(r) = r \ \text{ and } \ \psi^+(r) = \frac{1}{r}\frac{r_w^2 - r^2}{r_w^2 - 1}. \tag{16}$$

The solution (16) is represented in figure 3(*a*). To obtain the eigenfrequency ω^2, following [32], we can integrate equation (11) over an infinitesimal layer across $r = 1$, using the fact that $\varrho_{eq}(r)$ is a step function and that $J'_{eq}(r) = -2\delta(r-1)$. After straightforward algebra, we obtain the dispersion relation [32]

$$\omega^2 = \frac{2}{r_w^2 - 1} \tag{17}$$

which is the same as equation (7) for the normalized frequency $\omega^2 = \omega_{0c}^2\tau_A^2$ and for the dimensionless wall radius, with $a = b$ and $a_w = b_w$ for the circular case.

We note that ω^2 is a monotonically decreasing function of the wall radius r_w, and that it goes above unity for $r_w < \sqrt{3}$, see figure 3(*b*). The fact that the first of equation (15) is multiplied by $\left(\omega^2 - 1\right)$ should send warning signals. Indeed, if we focus on the coefficient of the second order derivative of ψ in equation (11), we find that it equals to

$$\frac{r^2\varrho_{eq}}{\psi'_{eq}}\left(\omega^2 - k_{||}^2v_A^2\right)\frac{\mathrm{d}^2\psi}{\mathrm{d}r^2} \ \text{ where } \ k_{||}^2v_A^2 = \frac{\psi'^2_{eq}}{r^2\varrho_{eq}} \tag{18}$$

$k_{||}$ is the wavevector component parallel to the equilibrium magnetic field and v_A is the Alfvén velocity. The profile of $k_{||}^2v_A^2$ for the equilibrium (13) is shown in figure 3(*c*). We see that $k_{||}^2v_A^2 = 1$ across the plasma, but it goes to infinity right at the plasma edge because of the plasma density jumping to zero at $r = 1$. Consequently, the coefficient $\left(\omega^2 - k_{||}^2v_A^2\right)$ changes sign, going from a positive value to $-\infty$, whenever ω^2 is larger than unity. This is evidence of the fact that, for the chosen equilibrium profiles, the VDOM interacts with the Alfvén continuum right at the plasma edge when $\omega^2 > 1$, i.e. when $r_w < \sqrt{3}$. This interaction should give rise to continuum damping.

Let us look more closely at what happens in a small interval of width 2ε, across the plasma boundary $1-\varepsilon < r < 1+\varepsilon$.

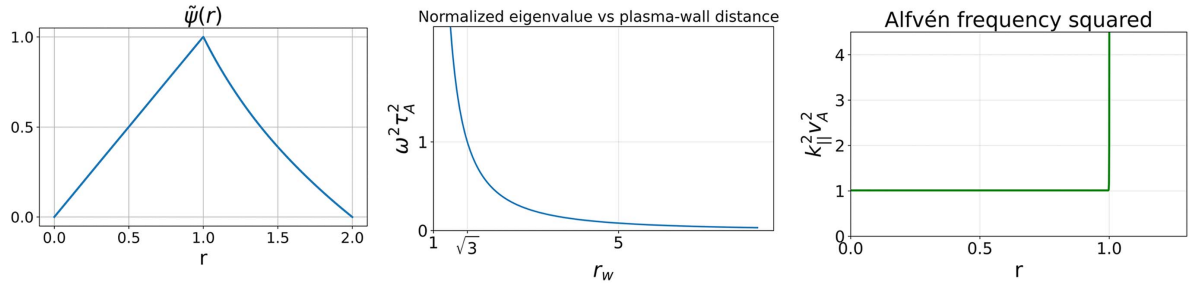

Figure 3. Solution of the normal mode equation in the circular cross section limit. (*a*) The perturbed flux as function of the normalized radius, Equation (16). (*b*) Normalized frequency square, ω^2, vs the normalized wall radius, equation (17). (*c*) Plot of $(k_\varepsilon v_A)^2$ vs the normalized radius, r, for the idealized equilibrium in equation (13).

Within this interval, we can approximate $\psi'_{eq} \approx r \approx 1$. Equation (11) becomes

$$\frac{d^2\psi}{dr^2} + \frac{\omega^2\varrho'_{eq}}{\omega^2\varrho_{eq}-1}\frac{d\psi}{dr} + \left(\frac{J'_{eq}}{\omega^2\varrho_{eq}-1} - 1\right)\psi = 0. \quad (19)$$

As we did before, we consider the integral of each of the terms of this equation with respect to r across the boundary, yielding four integrals:

$$I_1 = \int_{1-\epsilon}^{1+\varepsilon} \frac{d^2\psi}{dr^2} dr \quad (20)$$

$$I_2 = \int_{1-\epsilon}^{1+\varepsilon} \frac{\omega^2\varrho'_{eq}}{\omega^2\varrho_{eq}-1}\frac{d\psi}{dr} dr \quad (21)$$

$$I_3 = \int_{1-\epsilon}^{1+\varepsilon} \frac{J'_{eq}}{\omega^2\varrho_{eq}-1}\psi\, dr \quad (22)$$

$$I_4 = -\int_{1-\epsilon}^{1+\varepsilon} \psi\, dr. \quad (23)$$

The dispersion relation can be written as

$$I_1 + I_2\left(\omega^2\right) + I_3\left(\omega^2\right) + I_4 = 0. \quad (24)$$

The integrals I_1 and I_4 are real quantities, independent of ω^2; furthermore, I_4 is $\mathcal{O}(\varepsilon)$ compared with I_1 and therefore can be neglected. Likewise, neglecting corrections of $\mathcal{O}(\varepsilon)$, the evaluation of I_1 requires only the information of the outer solution $\psi^{\pm}(r)$ given by equations (16):

$$I_1 = \left|\frac{d\psi}{dr}\right|_{1-\varepsilon}^{1+\varepsilon} = -2 - \frac{2}{r_w^2-1} + \mathcal{O}(\varepsilon). \quad (25)$$

The integrals $I_2\left(\omega^2\right)$ and $I_3\left(\omega^2\right)$ exhibit a pole singularity whenever $\omega^2 \geqslant 1$. Let us focus at first on the principal parts, which can be evaluated for the equilibrium profiles (13) exploiting the fact that ϱ'_{eq} and J'_{eq} are delta-functions. Furthermore, we take $\varrho_{eq}(r=1) = 1/2$ and

$$\frac{d\psi}{dr}(r=1) = \frac{1}{2}\left(\frac{d\psi^+}{dr} + \frac{d\psi^-}{dr}\right)(r=1) = -\frac{1}{r_w^2-1}. \quad (26)$$

Then, we find

$$P(I_2) = \frac{1}{r_w^2-1}\frac{2\omega^2}{\omega^2-2} \text{ and } P(I_3) = -\frac{4}{\omega^2-2} \quad (27)$$

where $P(I)$ denotes the principal part of the integral. Then, it can be easily checked that $I_1 + P(I_2) + P(I_3) = 0$ is consistent with the dispersion relation (17).

The analytic evaluation of the pole contributions, and therefore of continuum damping, requires smoothing out the profiles of $\varrho_{eq}(r)$ and of $J_{eq}(r)$ around the plasma edge ($r=1$). It may be expected that the pole contribution, and therefore the continuum damping rate, will depend on the actual, smoothed-out profile. The detailed evaluation of continuum damping for realistic equilibrium profiles is left for a future publication. It should be noted, however, that the criterion $r_w < \sqrt{3}$ for the occurrence of continuum damping is only valid for the very special equilibrium, equations (13) and (14), adopted in this section. Numerical work, solving equation (11) by means of a shooting code, has shown that for a different type of equilibrium, e.g.

$$\varrho_{eq}(r) = \varrho_0\left(1-r^2\right)^2 \text{ and } J_{eq}(r) = J_0\left(1-r^2\right)^3 \quad (28)$$

the VDOM frequency remains below the minimum of even when the wall is brought to the plasma edge, $r_w \to 1$. It appears that the density profile plays an important role in determining whether VDOM is affected by continuum damping when the wall is very close to the plasma edge. We conjecture that for H-mode-like density profiles, where the density drops to zero rapidly in a narrow pedestal region near the plasma edge, VDOMs are more likely to be subject to continuum damping, albeit only when the wall is really close to the plasma edge, while for L-mode-like density profiles VDOMs are immune of continuum damping.

5. Impact of magnetic X-points

The analysis of the previous two sections assumed that the magnetic X-points of the simplified, double-null equilibrium configuration used for analytic work lie either outside the vacuum chamber, or, if inside, they lie in vacuum or in a cold, low-density halo plasma region. In reality, for a realistic tokamak divertor configuration, the hot plasma extends to the magnetic separatrix (the last-closed-magnetic-surface), where the X-points are located. As discussed in [12] based on analytic considerations, and shown numerically in [34], the most likely consequence is that axisymmetric current sheets

localized around the magnetic X-points and extending along the magnetic separatrix are driven by $n = 0$ perturbation. In [12] it was concluded that these X-point current sheets, which become singular with a vanishing width in the ideal-MHD limit, can have a stabilizing effect on vertical plasma displacements. However, the theory of [12] did not consider resistive effects, which can resolve the ideal-MHD singularity, providing a characteristic width for the X-point current sheets. This problem is as yet unresolved. It is nevertheless a very relevant issue, since these X-points current sheets can have a profound impact on plasma edge stability (e.g. on the stability of peeling-ballooning modes leading to ELMs). Furthermore, they are likely associated with axisymmetric sheared flows, which can affect the turbulent transport of plasma particles and energy across the plasma edge and into the open field line region.

Magnetic X-points give rise to singularities in the ideal-MHD limit because the parallel wave-vector operator, $k_{||} = \mathbf{b}\cdot\nabla$, where $\mathbf{b}$ is the unit vector along the equilibrium magnetic field, vanishes identically for mode number $n = 0$, since the poloidal component of the equilibrium magnetic field vanishes on the X-points. The resonance involves the toroidal field line going through magnetic X-points. Because of this resonant and singular behaviour, ideal-MHD becomes a poor representation of the plasma dynamics for axisymmetric perturbations in the vicinity of magnetic X-points. A better model involves dissipation and other extended-MHD effects, such as two-fluid effects, finite ion Larmor radius, and a generalized Ohm's law. Besides the mentioned analytic work [12], X-point current sheets have been observed in tokamak experiments [35, 36] and in numerical simulations [34, 37].

6. Fast particle drive

GAM, GAE, and VDOM have in common that they can all be destabilized by their resonant interaction with fast ions, the relevant resonance condition is $\omega = p\omega_{t/b}$, where $\omega_{t/b}$ is the transit/bounce frequency of fast ions with passing/trapped orbits. GAM, being relatively low-frequency perturbations, can be destabilized by fast ions in the 20–100 keV range, arising, for instance, by NBI in current day devices; this energetic-particle-induced GAM, or EGAM, was first discussed in [14]. The driving of GAE [5] and of VDOM [1] require instead fast ions with energy ranging from 100 keV to a few MeV. Nevertheless, the fast particle drives for all these modes have an important element in common: since $n = 0$, the part of the perturbed fast ion distribution function that involves derivatives of the orbit averaged equilibrium fast ion distribution, f_h with respect to the toroidal canonical momentum, $\partial f_h/\partial P_\varphi$, being multiplied by the toroidal mode number, is absent (see, e.g. [38]). Furthermore, the mode frequencies associated with the $n = 0$ modes are well below the ion cyclotron frequency of the energetic ions resonating with them. Consequently, the wave-particle interaction leaves the magnetic momentum, $\mu = mv_\perp^2/2B$, unaffected. A positive drive for $n = 0$ therefore requires bump-on-tail-like equilibrium distribution functions in the direction of phase space in which μ is constant; more specifically, in at least some regions of phase space, a necessary condition for fast particle destabilization of $n = 0$ modes is

$$\left.\frac{\partial f_h}{\partial \varepsilon}\right|_\mu = \left.\frac{\partial f_h}{\partial \varepsilon}\right|_\Lambda - \frac{\Lambda}{\varepsilon}\left.\frac{\partial f_h}{\partial \Lambda}\right|_\varepsilon > 0 \tag{29}$$

where $\varepsilon = mv^2/2$ is the particle kinetic energy and $\Lambda = \mu B_0/\varepsilon$ is the pitch angle variable, with B_0 the on-axis magnetic field. An isotropic distribution function in velocity space does not depend on Λ in the small banana width limit. Thus, in this limit the standard, isotropic slowing-down distribution function for the fast ions, being monotonically decreasing as function of energy, does not satisfy equation (29). This may explain why $n = 0$ saturated fluctuations are observed in tokamak experiments sometimes only transiently, for instance after sawtooth crashes [6, 39], or when NBI heating is modulated or ramped up [6, 40], as a fully developed slowing down distribution requires a time to form or be recreated of the order of the slowing-down time.

While equation (29) is a necessary condition, the complete picture is more complicated. The main purpose of this section is to illustrate factors that play a key role for the drive of $n = 0$ modes that may not have been made very explicit before. To this end, we employ simplified modelling, which makes it easier to investigate the role of such factors as compared to studying results of more comprehensive modelling.

An analysis of the linear growth rate of $n = 0$ modes yields [1, 41],

$$\lambda_h = \frac{8\pi^4}{W_{inst}}\omega\sum_\sigma\iint\sqrt{g}\sum_p|L_{1,p}|^2\left(p\frac{\partial\omega_{t/b}}{\partial\varepsilon}\right)^{-1}\left(\frac{\partial f_h}{\partial\varepsilon}-\frac{\Lambda}{\varepsilon}\frac{\partial f_h}{\partial\Lambda}\right)\Bigg|_{\varepsilon=\varepsilon_p^*}$$
$$\mathrm{d}\Lambda\mathrm{d}P_\varphi = \varsigma\int\sum_p\bar{\lambda}'_{h,p}dP_\varphi \tag{30}$$

where λ_h is the normalized growth rate parameter defined such that $\gamma_h = \omega\lambda_H/2$, $\sqrt{g} = \varepsilon/\left(ZeB_0m^2\omega_{t/b}\right)$ (the Jacobian in the variables $\varepsilon, \Lambda and P_\varphi$), W_{inst} is the kinetic energy of the instability wave, $|L_{1,p}|$ is the absolute value of the perturbed Lagrangian and ε_p^* is the resonant energy implicitly given by $\omega = p\omega_{t/b}(\varepsilon_p^*, \Lambda, P_\varphi)$ and $\varsigma = 16\pi^4 p/\left(\omega ZeB_0m^2\right)$. For a definition of the perturbed Lagrangian, see equation (37) below.

To develop intuition for how the expression above works, two types of anisotropic fast ion distributions are of interest: NBI and acceleration of ions by ICRF (Ion Cyclotron Range of Frequencies) waves. In large tokamaks, one must use very high injection energies for the beams to penetrate to the central regions of the plasma, in ITER typically one MeV, and at such energies the pitch angle scattering is very weak. Consequently, in the high energy range, the distribution function of injected ions will be narrow in the Λ direction and centred around Λ_0, which is the value of Λ at the point of ionization. In the case of energetic ions accelerated by ICRF waves, they tend to pile up with their Λ values around $\Lambda_{\mathrm{IC}} = B_0/B_{\mathrm{IC}}$, where the magnetic field B_{IC} is defined by $n_{\mathrm{ic}}\omega_{ci}(B_{\mathrm{IC}}) = \omega_{\mathrm{IC}}$, n_{ic} is the harmonic number of the ICRF resonance, ω_{ci} is the ion cyclotron frequency and ω_{IC} is the frequency of the injected

fast magneto-sonic wave. The reason for this is that the resonating ions are mainly accelerated in the perpendicular direction and stay resonant only until they have their turning points in the vicinity of the unshifted cyclotron resonance. To see more easily how the anisotropy in Λ can lead to a destabilization of $n=0$ modes, we will adopt here the small banana width limit (i.e. $P_\varphi \approx Ze\psi$). As a rough approximation, a 'mock-up' distribution function for both NBI and ICRF cases is of the type,

$$f_h = F_h(\varepsilon,\psi)\, d(\Lambda-\Lambda_h) \tag{31}$$

will be used, where we replace h with 'NB' and 'IC' when dealing with a distribution representing NBI injected ions and ICRF accelerated ions, respectively; the function $d(\Lambda-\Lambda_h)$ is given by,

$$d(\Lambda-\Lambda_h) = \frac{1}{\sqrt{\pi}\,\Delta\Lambda}\exp\left[-\left(\frac{\Lambda-\Lambda_h}{\Delta\Lambda}\right)^2\right]. \tag{32}$$

In reality, $\Delta\Lambda$ is energy dependent because the pitch angle scattering increases as the energy decreases. However, for the sake of simplicity, taking into account that for small $\Delta\Lambda$ the function d needs to be representative of the actual width only in the neighbourhood of the resonant energy $\varepsilon=\varepsilon_p^*(\omega,\Lambda_h,\psi)$, energy dependence of $\Delta\Lambda$ is neglected in what follows.

In the case of NBI injection, $F_h(\varepsilon,\psi)$ would simply be given by the classical slowing down distribution and for high energy NBI (like, for instance, 1 MeV beams in ITER) one may even neglect ion collisions in the high energy range, and for illustration we will here simply use,

$$F_{\rm NB}(\varepsilon,\psi) = \begin{cases} \frac{C_{\rm NB}}{\varepsilon^{3/2}} & \varepsilon<\varepsilon_0 \\ \frac{C_{\rm NB}}{\varepsilon_0^{3/2}} exp\left[-\frac{\varepsilon-\varepsilon_0}{T_e}\right] & \varepsilon>\varepsilon_0 \end{cases} \tag{33}$$

where $C_{\rm NB}$ is a constant (depending on ψ) proportional to the NBI source density and the ion-electron slowing down time and ε_0 is the injection energy. Even if collisional energy diffusion is weak at high energies; it nevertheless gives rise to a slope of the distribution function above the injection energy roughly determined by the electron temperature (because collisions with electrons dominate at high energies). For this reason, it is necessary to account for the distribution for $\varepsilon>\varepsilon_0$ not least to avoid an infinite energy derivative in equation (29) at $\varepsilon=\varepsilon_0$. In the following we denote $\Lambda_h=\Lambda_0$ for the NBI case.

In the case of ICRF heated energetic ions their distribution can be approximated by a Maxwellian with a high tail temperature,

$$F_{\rm ICRF}(\varepsilon,\psi) = C_{\rm IC}\exp\left(-\frac{\varepsilon}{T_{\rm tail}}\right) \tag{34}$$

where $C_{\rm IC}$ is a constant (depending on ψ) proportional to the density of non-thermal resonating ions.

For the type of model distributions above, there will be both contributions to the damping ($\Lambda<\Lambda_h$) and the drive ($\Lambda>\Lambda_h$) of $n=0$ modes from the $\partial f_h/\partial\Lambda$ term in equation (29). For this reason, the key factor for the drive of the mode is the interaction strength between the mode and the energetic ions on either side of Λ_h. If the energy exchange is stronger for $\Lambda>\Lambda_h$ than for $\Lambda<\Lambda_h$, there can be positive contribution to the drive of the mode provided the damping effect of the $\partial f_h/\partial\varepsilon$ term can be overcome. Let us now introduce the function G_p defined as,

$$G_p\left(\varepsilon_p^*,\Lambda,\psi\right) = \frac{8\pi^4}{W_{inst}}\omega\sqrt{g}\,|L_{1,p}|^2\left(p\frac{\partial\omega_{t/b}}{\partial\varepsilon}\right)^{-1}\frac{\Lambda}{\varepsilon}F_h(\varepsilon,\psi)|_{\varepsilon=\varepsilon_p^*} \tag{35}$$

which is the term multiplying $\partial f_h/\partial\Lambda$. in equation (29). Thus, if this quantity has a positive Λ derivative in the neighbourhood of $\Lambda=\Lambda_h$, then, for a narrow distribution function in the Λ direction, there is a positive contribution to the drive of $n=0$ modes. In other words, the necessary condition for having a positive contribution from the $\partial f_h/\partial\Lambda$ term to the drive of $n=0$ modes in the limit of small $\Delta\Lambda$ is

$$\frac{\partial G_p\left(\varepsilon_p^*,\Lambda,P_\varphi\right)}{\partial\Lambda}|_{\Lambda=\Lambda_h}>0. \tag{36}$$

As we will see, for lager $\Delta\Lambda$ the situation is more complicated. Nevertheless, the key to understanding the drive of $n=0$ modes for anisotropic distributions considered is the behaviour of G_p around Λ_h, rather than simply equation (29), since the $\partial f_h/\partial\Lambda$ term will always give a positive contribution to $\lambda'_{h,p}$ when $\Lambda>\Lambda_h$.

If the derivative in equation (36) is sufficiently large, the damping contribution from the $\partial f_h/\partial\varepsilon$ can be overcome, and the mode will be excited. Hence, to better understand the conditions for driving the mode for the two cases of interest (NBI and ICRF), it is instructive to plot $G_p\left(\varepsilon_p^*,\Lambda,\psi\right)$ for the two mock-up distributions. We turn our attention to VDOM and limit the study to the fundamental resonance $p=1$. For VDOM, the perturbed Lagrangian is caused by the perturbed electric field associated with the mode on the vertical (drift) motion of the energetic ions. One finds approximately [1, 41]

$$|L_{1,1}| \approx \left|\frac{1}{\tau_b}\int_0^{\tau_b}\varepsilon\left(2-\Lambda\frac{B}{B_0}\right)\vec{\xi}\cdot\vec{\kappa}e^{i\omega_b\tau}d\tau\right| \tag{37}$$

Where $\vec{\xi}$ is the displacement vector and $\vec{\kappa}$ is the magnetic curvature vector. This expression has been evaluated numerically for NBI and ICRF cases. In the case of NBI, a device with a major radius of six metres has been assumed together with an injection energy of 1 MeV (representative of ITER) and for simplicity circular flux surfaces are employed. We start by considering a flux surface with $r/R_0=0.05$, and an instability frequency of $\omega/(2\pi)=150$ kHz. In figure 4(*a*) the resulting normalized growth rate parameter $\bar{\lambda}'_{h,1}$, is shown as a function of $\Lambda_{\rm inj}$ for three different widths $\Delta\Lambda$; while figure 4(*b*) shows and resonant energy, ε_1^*, as functions of Λ. Note that the impact of the $F_h(\varepsilon,\psi)$ on G_1 and $\bar{\lambda}'_{h,1}$ is very strong because it must be evaluated at the resonant energy ε_1^*, which is Λ dependent. In figure 4(*b*) one can see that $\varepsilon_1^*=\varepsilon_0$ at around $\Lambda\approx0.66$. For Λ values below 0.66 the derivative of G_1 with respect to Λ is positive. This can easily be understood because

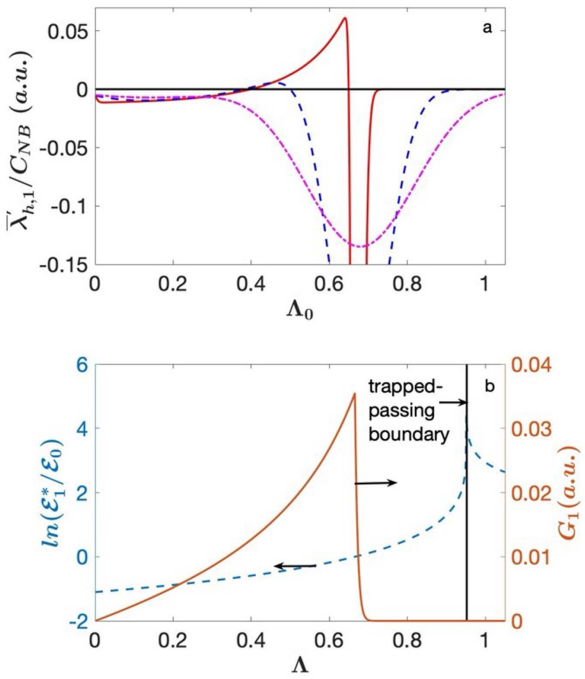

Figure 4. NBI mock-up case for $r/R_0 = 0.05$. (a) Normalized $\bar{\lambda}'_{h,1}$ as function of Λ- for three different widths $\Delta\Lambda$: 0.01, solid line; 0.1, dashed line; 0.2 dot-dashed line; (b) resonant energy over injection energy as function of Λ, dashed line; G. for $p = 1$ as function of Λ, solid line.

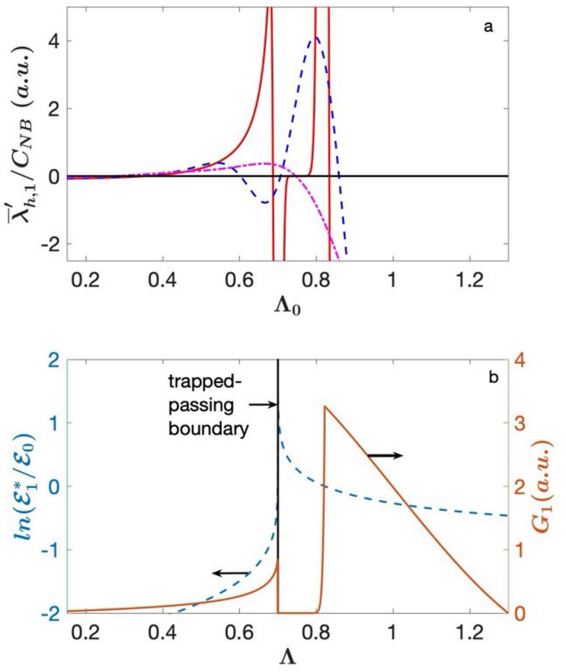

Figure 5. NBI mock-up case for r/R- $= 0.3$ (a) normalized $\bar{\lambda}'_{h,1}$ as function of Λ- for three different widths $\Delta\Lambda$: 0.01. solid line; 0.1, dashed line; 0.2, dot dashed line; (b) resonant energy over injection energy as function of Λ, dashed line; G. for $p = 1$ as function of Λ, solid line.

the transit frequency of passing particles decreases with Λ at constant energy and the condition $\omega = \omega_{t/b}$ then requires ε_1^* to rise as Λ increases. The main reason for the increase of G_1 with Λ in the passing region is that $L_{1,1}$ is proportional to ε_1^*. Consequently, for a sufficiently small width $\Delta\Lambda$ the $\partial f_h/\partial\Lambda$ in term equation (30) will contribute to the drive of the VDOM. In the case of the smallest width, $\Delta\Lambda = 0.01$, the driving contribution from the $\partial f_h/\partial\Lambda$ term overcomes the damping caused by the $\partial f_h/\partial\varepsilon$ term at $\Lambda \approx 0.4$ (which is consistent with what one finds analytically for a delta function distribution in the direction using approximate expressions for the quantities in equation (30) valid for passing particles not too close to the passing-trapped boundary). In the case of $\Delta\Lambda = 0.1$, a significant part of the distribution in the Λ direction rapidly passes into the region where $\varepsilon_1^* > \varepsilon_0$ as Λ_0 approaches 0.66 and contribution to the drive is gradually diminished such that it is positive only up to a Λ_0 of around 0.5. When the width is further increased to $\Delta\Lambda = 0.2$, not enough of the distribution in the Λ direction lies in the region between 0.4 and 0.6 for the damping of the mode to be overcome by the positive contribution from the part of the distribution with. Hence, figure 5(a) indicates that for an NBI type of distribution function there is potential for the drive of a VDOM if Λ is grater or of the order of 0.4, but that the results depend rather sensitively on the width of the distribution in the Λ direction.

In a device like ITER, Λ_0 would correspond to injection of passing ions at $r/R_0 = 0.05$. However, towards the edge of the plasma Λ_0 could lie in the trapped region and to study such cases we consider $r/R_0 = 0.3$. Because the bounce frequency, $\omega_{t/b}$, for trapped ions is lower than the transit frequency for passing ions at the same energy, it is necessary to lower the mode frequency to find resonances with trapped ions and here we consider $\omega/(2\pi) = 70\,\mathrm{kHz}$. This may be less relevant than for the case with more central flux surfaces, and one can of course debate if the frequency is compatible with a VDOM at the edge, but it illustrates the complexity of the behaviour of $\bar{\lambda}'_{h,1}$ when Λ_0 moves into the trapped region. The result is shown in figure 5 and one can see that between the trapped-passing boundary and up to Λ around 0.8 the resonance energy, ε_1^*, is above the injection energy and consequently G_1 is zero in this region. For the case of the narrowest distribution Λ this means that as Λ_0 moves into the trapped region $\lambda'_{h,1}$ becomes equal to zero, but as Λ increases the resonance energy goes down and effective interaction takes place only again when the Λ distribution extends to values of Λ greater than or approximately equal to 0.8. At first there is then a positive contribution to $\lambda'_{h,1}$ from the $\partial f_h/\partial\Lambda$ term. However, the situation is complicated by the fact that there is a significant contribution from the $\partial f_h/\partial\varepsilon$ term for Λ values such that the resonant energy ε_1^* is just above the injection energy (i.e. where the distribution drops off with slope determined by the electron temperature in our model distribution function). Nevertheless, the contribution from the $\partial f_h/\partial\Lambda$ term dominates leading to $\bar{\lambda}'_{h,1} > 0$, i.e. there is a positive contribution to the drive. As

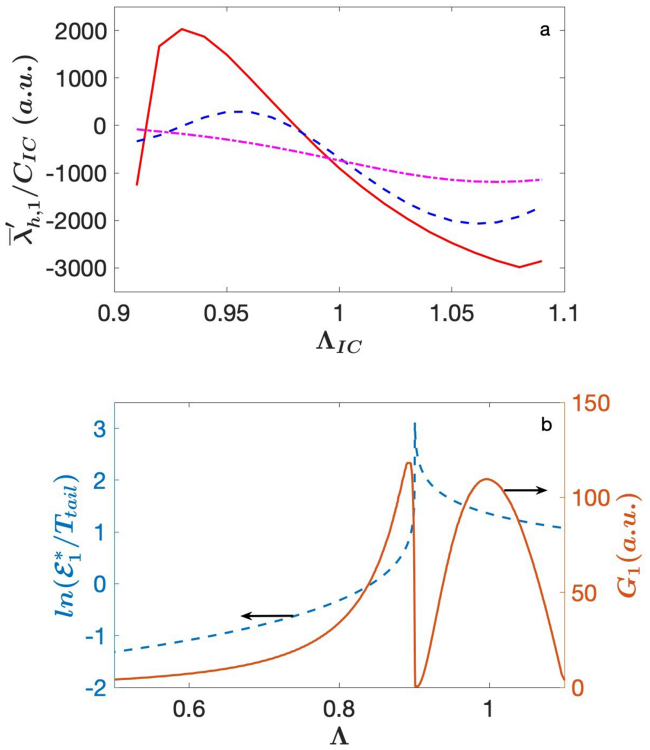

Figure 6. ICRF mock-up case, (*a*) Normalized $\bar{\lambda}'_{h,1}$ as a function of $\Lambda_{\rm IC}$ for three different widths: $\Delta\Lambda$: 0.01 solid line, 0.05 dashed line, 0.1, dot-dashed line; (*b*) Resonant energy over tail temperature as a function of Λ, dashed line; the function G_p for $p = 1$ as a function of, Λ solid line.

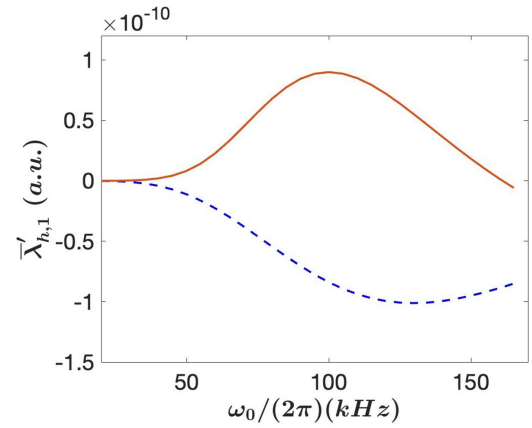

Figure 7. Normalized VDOM fast particle drive λ_h for $p = 1$ (see equation (7)), obtained with distribution functions from PION simulations of a JET sized plasma with $P_{\rm RF} = 6$ MW for hydrogen minority heating $(H)D$, $n_H/n_D = 4\%$.The solid line corresponds to a high field side ICRF resonance about 30 cm from the magnetic axis, while the dashed line corresponds to a low field side resonance with a similar distance from the magnetic axis. In this example λ_h was evaluated for a flux surface intersecting the midplane at a radius of around 35 cm.

Λ_0 is increased further, beyond $\Lambda \approx 0.84$, most of the Λ distribution is in the region where decreases with Λ leading to $\lambda'_{h,1} < 0$. For the intermediate width of $\Delta\Lambda$ the situation is similar, but in this case the Λ distribution is wider that the region in which $\varepsilon_1^* > \varepsilon_0$ leading to wider span of Λ_0 for which $\bar{\lambda}'_{h,1} > 0$, i.e. a positive contribution to the drive of the mode. For the widest Λ distribution, $\Delta\Lambda = 0.2$, the contribution from $\partial f_h/\partial\Lambda$ is not enough to overcome the damping associated with $\partial f_h/\partial\varepsilon$ term. This is because of the width of the Λ distribution is not sufficiently concentrated to the region where G_1 is maximum in the trapped region.

Turning to the ICRF type of distribution above, a device with a major radius of three metres is assumed together with ICRF accelerated hydrogen ions having a tail temperature of 1 MeV, which is in a range that was normal at JET. The contribution to from a flux surface with $r/R_0 = 0.1$ has been studied for an instability frequency of $\omega = 120$ kHz. On this flux surface $\Lambda_{\rm IC}$ can range from 0.9–1.1, with the resonance $\omega_{\rm IC} = \omega_c$ (ICRF wave frequency equal to the cyclotron frequency of the resonating species) being tangent to the flux surface on the high field side at $\Lambda_{\rm IC} = 0.9$; while $\Lambda_{\rm IC} = 1$ corresponds to an on-axis resonance. As can be seen from figure 6(*b*), there is a potential for a drive of the VDOM mainly if $\Lambda_{\rm IC}$ is roughly between 0.9 and 1.0. Consequently, the results show that a drive of VDOM modes is privileged by high field side resonances, which is discussed in more detail in [28]. Again, there is a considerable sensitivity to the width, $\Delta\Lambda$, of the distribution function. Because the width of the distribution in the Λ direction varies strongly with the energy for ICRF accelerated ion, it is of interest to test more realistic calculations of the distribution function. To this end we have used the PION code augmented with a package for better assessing the anisotropy of the distribution function [41]. The code has been run for typical parameters of a JET-sized plasma with 6 MW of ICRF power. Two cases have been analysed. In the first case, the ICRF resonance was about 30 cm to the low field side of the magnetic axis, and in the second case around 30 cm to the high field side (as measured in the mid-plane). The resulting normalized growth rate parameter, $\bar{\lambda}'_{h,1}$ as a function of the instability frequency is shown in figure 7 for the two cases from a flux surface with a radius of approximately 35 cm in the midplane is shown in figure 7. As can be seen, consistent with the analysis above, the ICRF accelerated ions has potential to drive the VDOM for high field side resonances while no drive is found for low field side resonances for the instability frequencies considered.

The results presented so far have been obtained by considering the narrow orbit width limit. It is therefore of interest to assess the impact of finite orbit width effects. They should be mostly of importance for trapped ions, i.e. for the ICRF case discussed above. We have therefore calculated the bounce frequency and the perturbed Lagrangian with and without finite orbit width effects for particles with the same P_φ, corresponding to having turning points on the flux surface $r/R_0 = 0.1$ for the ICRF case. The calculations have been made for hydrogen ions with an energy of 1 MeV (it has been assumed that the displacement ξ is approximately constant over the

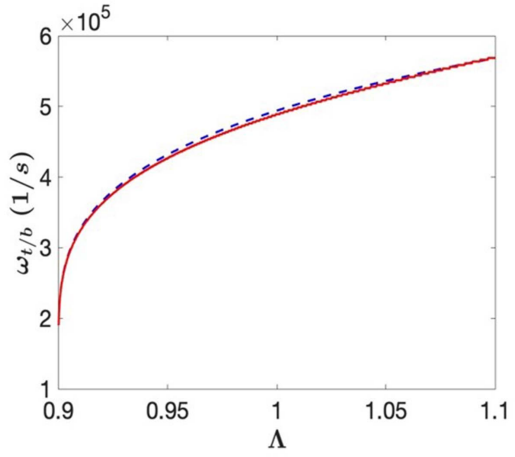

Figure 8. Bounce frequency of trapped ions with turning points on a flux surface with $r/R_0 = 0.1$; small banana width limit, dashed line; finite orbit width, solid line.

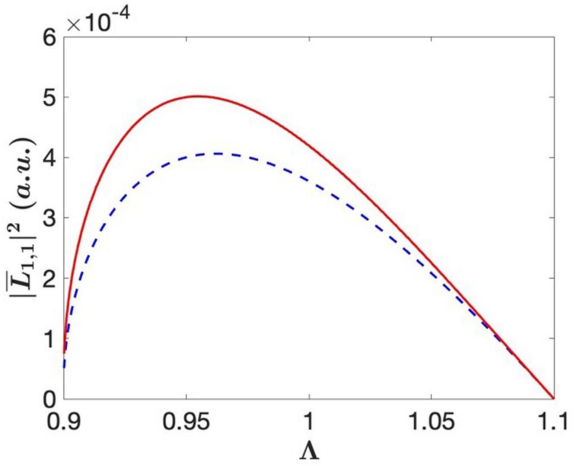

Figure 9. Normalized (by ε and ξ) perturbed Lagrangian on a flux surface with $r/R_0 = 0.1$; small banana width limit, dashed line; finite orbit width, solid line.

radius covered by the energetic ions). The results are shown in figures 8 and 9. One can see that the bounce frequency is not much affected by the finite orbit width while the perturbed Lagrangian is somewhat higher when finite orbit width effects are taken into account. However, the difference is not too significant and will not qualitatively alter the conclusions obtained from the calculations using the small orbit width limit for the case presented in figure 7. Nevertheless, for flux surfaces nearer the centre of the plasma, finite orbit width effects become important when the banana width is comparable with the distance from the magnetic axis. Furthermore, fusion born alpha particles have significantly wider orbits than the 1 MeV hydrogen orbits considered in figures 8 and 9 and finite orbit width effects should therefore have a much greater impact on their interaction with $n = 0$ modes. One should also note that with a peaked isotropic birth source, the resulting alpha particle distribution function expressed in the variables ε, Λ and P_φ will exhibit a significant variation with Λ in the trapped region because of finite orbit width effects, which could lead to a positive contribution to the drive of $n = 0$ modes.

An important conclusion of this section is that the width of the energetic ion distribution in the Λ direction plays a crucial role in determining whether there is positive contribution to the drive of modes and the strength of it. This indicates that for a realistic assessment of the drive of $n = 0$ modes it is necessary to use reasonably detailed calculations or models of the energetic ion distribution functions. However, the key takeaway is the crucial role played by the behaviour of the function G_p around Λ_h. Because there will always be a region where $\partial f_h/\partial\Lambda < 0$ for energetic ions associated with NBI and ICRF, it is the-variation of G_p that determines if there is an overall positive contribution to the drive of a VDOM.

7. Numerical simulations

The analytic theory of VDOM, developed based on simplified straight-tokamak equilibria and reviewed in section 2 has been confirmed by numerical simulations [34]. Furthermore, the physics features that characterize VDOMs, such as the perturbed flow and magnetic field spatial structure, external mode character, and frequency dependence on plasma-wall distance, have been recognized in numerical simulations using the NIMROD code adopting realistic tokamak geometry and equilibrium profiles [11]. NIMROD [42] is a 3D, initial value, extended-MHD code that allows for the treatment of a 'halo' plasma region (low-density, low-temperature) that extends beyond the last-closed-flux-surface to the plasma wall. This open field line 'halo' region is particularly important for the study of VDOM, an external plasma mode that relies on the interaction between the axisymmetric, vertically oscillating plasma current and the induced currents on the plasma wall.

In the first part of this Section, we review how VDOM are identified in stable linear simulations and report on stable linear analysis of JET discharge #104408 from the last DT3 campaign [7, 8] where high frequency $n = 0$ modes driven by fusion alpha particles, rather than energetic particles from NBI or ICRF, were first observed. In the second part of this Section, we present preliminary simulations of $n = 0$ VDOM driven unstable by fast particles having a bump on-tail distribution using the δf Particle-in-Cell (PiC) module in NIMROD [43].

Identification of a stable normal mode in an initial value code is complicated because a typical initial condition with a generic perturbation will perturb all sorts of normal modes as well as continuum Alfvén quasi-modes. This differs from unstable modes, which are easily identified in initial value codes due to their exponential growth while the mode amplitude is still relatively small (i.e. the linear phase). To identify the stable VDOM, the Fast Fourier Transform (FFT) is employed to analyse the temporal behaviour of the plasma. FFT is applied to localized point probes that record the temporal evolution of the simulated plasma fields. By comparing the FFT spectra from multiple point probes in the simulation domain, we identify frequencies of interest where the

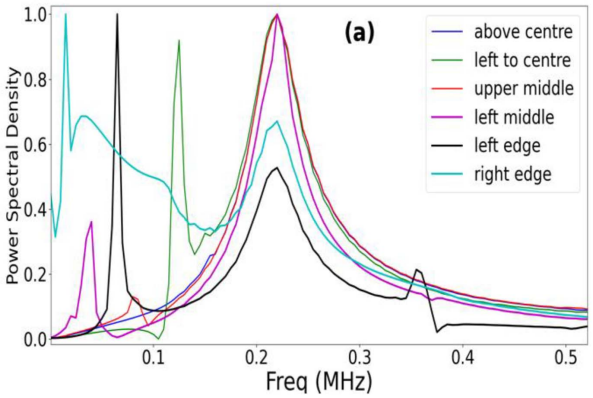

Figure 10. FFT spectra of the perturbed velocity in the vertical (Z) direction from six poloidal locations. The left panel (a) corresponds to a case with halo currents, showing a coherent peak at $f \sim$217 kHz, with all probes around that frequency oscillating in a synchronous way, suggesting the presence of a normal mode. The right panel (b) shows a distinct spectrum for each probe with no common frequency peaks.

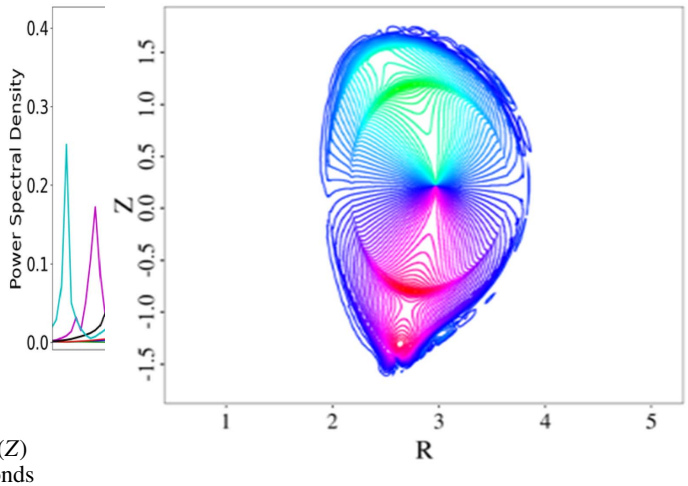

Figure 11. Contour plot of poloidal projection of the flux normal component of the $n = 0$ plasma velocity. This coherent $m = 1$ structure oscillates in time at the VDOM frequency.

FFT spectra align. An alignment of multiple, spatially distributed probes at a particular frequency suggests a spatially coherent oscillation, i.e. a normal mode. Figure 10 shows two examples of FFT spectra of the perturbed velocity in the vertical (Z) direction from six poloidal locations. The left panel (figure 10(a)) shows a case with a halo plasma region of width $0.15a$, while the right panel (figure 10(b)) shows a case without a halo plasma region. Figure 10(a) shows a coherent peak at $f \sim$217 kHz. Figure 10(b) shows a distinct spectrum for each probe with no common frequency peaks. Once a frequency of interest is identified, we run a second simulation with an applied external oscillator that mimics the injection of a wave at the frequency of interest. If the driving frequency is a normal mode, the NIMROD simulation will respond with an oscillating coherent mode as shown in figure 11, which is a contour plot of the poloidal projection of the flux normal component of the $n = 0$ plasma velocity. This coherent $m = 1$ structure oscillates in time at the VDOM frequency. This stable linear analysis method in NIMROD was first reported in [11].

Having elucidated how we can identify the presence, frequency and mode structure of a VDOM in numerical simulations even in the absence of the fast particle drive, we now turn to simulations of VDOM in JET discharge #104408 from the last DT3 campaign [7, 8]. With an ideal conducting wall placed at the separatrix, NIMROD finds a mode which can be either a GAE or a VDOM. To distinguish between the two, we have performed scans in the density pedestal gradient as well as in the plasma-wall distance. The results are shown in figures 12 and 13.

Scans in the density pedestal gradient were performed with a fixed wall placed at the separatrix. Figure 12(a) shows the density profiles for pedestal gradients $\mathrm{d}\ln(n0)/\mathrm{d}x = (5.0, 9.0, 34.5)\ m^{-1}$. Figure 12($b$) plots the VDOM frequency as a function of the density pedestal gradient (open circles correspond to the three profiles of figure 12(a), going from the less steep at higher frequency to steeper at lower frequency). As the steepness of the pedestal density gradient increases, the frequency is observed to decrease.

The shape of the plasma boundary can be described by the function $r(\vartheta)$, which is the distance between the magnetic axis and the plasma boundary as function of the standard poloidal angle ϑ. Likewise, we can define the function $r_{\mathrm{w}}(\vartheta)$ that corresponds to the distance between the magnetic axis and the wall. In the plasma-wall scan, the wall shape used in the NIMROD simulations presented in figure 13 corresponds to values of the normalized plasma-wall distance $\delta = [r_{\mathrm{w}}(\vartheta) - r(\vartheta)]/r(\vartheta)$ that are independent of the angle ϑ.

Figure 13(a) shows the radial profiles of the $n = 0$ poloidal magnetic field for different values of the normalized plasma-wall distance δ. The $n = 0$ normalized poloidal magnetic field profile is plotted along a radial chord on the poloidal midplane going from the magnetic axis ($\wp = 0$) to the separatrix ($\wp = 1$). As the wall is moved away from the last closed flux surface, the normalized local response at the pedestal becomes less peaked, while the frequency of the $n = 0$ mode decreases. A realistic value for the wall-separatrix normalized distance in the relevant JET experiments is 0.25, for which NIMROD finds the frequency 185 kHz. These results are in fair agreement with experimental observations and lend support to the interpretation of the mode observed at JET as a VDOM.

Finally, we present preliminary numerical results of $n = 0$ VDOM driven unstable by fast particles having a bump-on-tail distribution function. We use the hybrid kinetic-MHD module in NIMROD [43] to perform linear simulations of VDOMs excited by energetic ions. The module adopts a PiC method and the δf method to linearly push particles and reconstruct the perturbed fast particle distribution function, which is then used to calculate the fast particle pressure tensor within a standard hybrid kinetic-MHD approach. For this VDOM study, the energetic particle module has been modified to use a Maxwellian shifted in the parallel velocity direction, which gives rise to a bump-on-tail distribution in the energy direction when the magnetic momentum, μ, is kept constant. The resulting distribution is parametrized by a Gaussian width, V_{thermal},

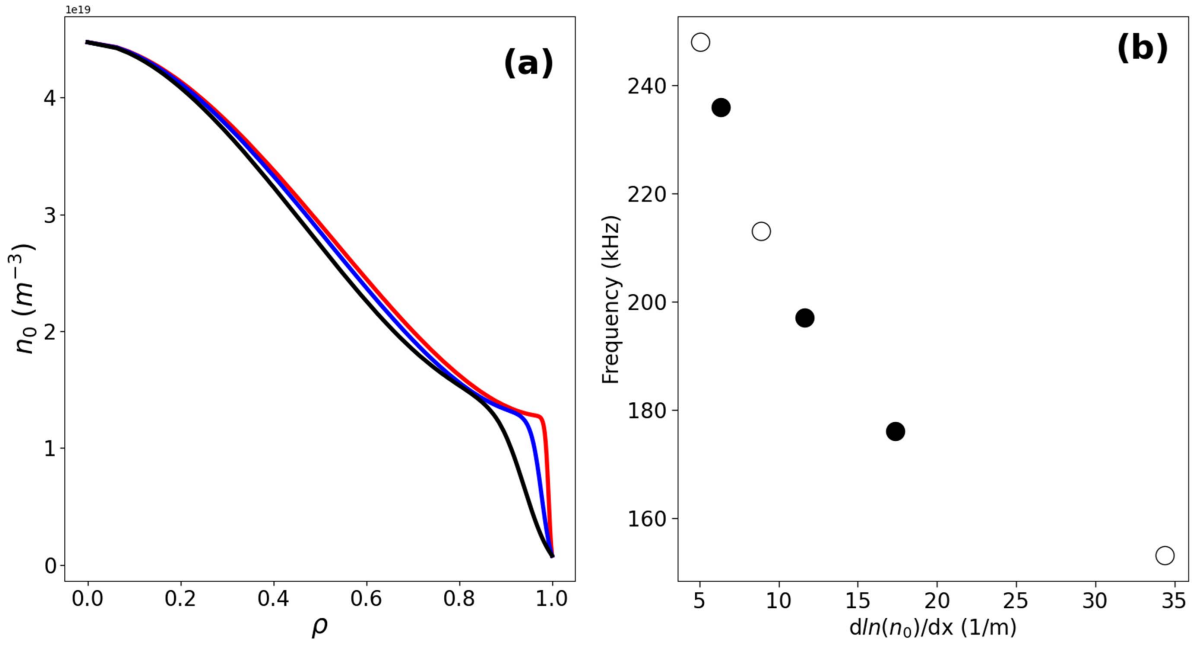

Figure 12. Density pedestal gradient scan. (*a*) shows the equilibrium density profiles for pedestal gradients dln(*n*0)/d*x* = (5.0, 9.0, 34.5) m^{-1}]. b). (*b*) plots the VDOM frequency as a function of density pedestal gradient (the three open circles correspond to the three profiles in (*a*)). As the steepness of the pedestal density gradient increases, the frequency is observed to decrease.

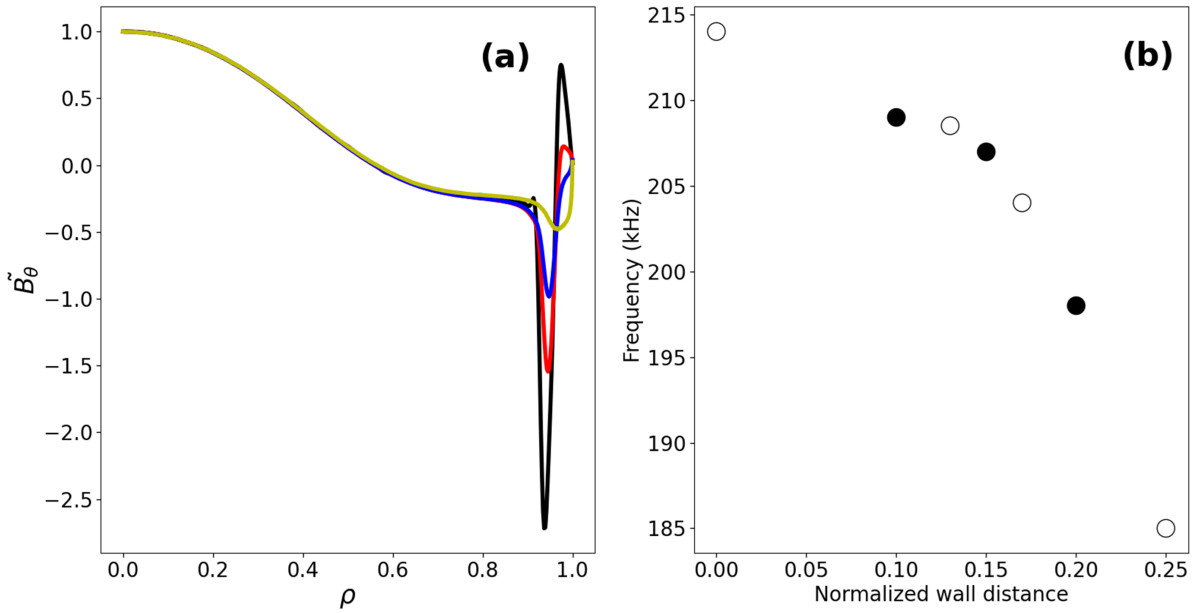

Figure 13. Normalized wall-distance scan. (*a*) Radial profile of the $n = 0$ poloidal magnetic field perturbation as the normalized plasma-wall distance parameter δ changes. (*b*) Frequency vs normalized plasma-wall distance. The four open circles in part (*b*) correspond to the four profiles in part (*a*). As the wall is moved away from the last closed flux surface, the relative local response near the pedestal becomes less peaked and the frequency of the $n = 0$ mode decreases.

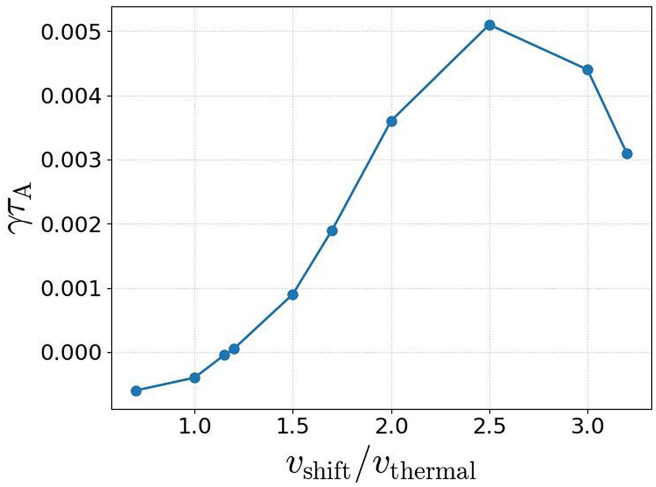

Figure 14. Plot of the linear growth rate as a function of the velocity shift normalized by the thermal velocity.

and a displacement in the parallel velocity, $V_{\rm shift}$. Equation (38) shows shifted bump-on-tail distribution,

$$F_h = Cv_{\rm therm}^{-3}\exp\left(-\frac{P_\varphi}{\psi_n}-\frac{\left(v_{||}+v_{\rm shift}\right)^2+v_\perp^2}{v_{\rm therm}^2}\right) \qquad (38)$$

where P_φ is the toroidal canonical momentum, ψ_n is one-quarter of the total magnetic flux, and C is a normalization constant that ensures a prescribed value of the fast particle beta, β_h. For the simulations reported here, we have chosen $\beta_h = 0.01\beta_{\rm MHD}$. As an initial demonstration of energetic particle excitation of the VDOM, we start with JET shot #102371, which was studied in [11]. These linear hybrid kinetic-MHD simulations use 2M particles and similar parameters to those used in the NIMROD simulations of [11]. Unlike the stable oscillations demonstrated in [11], these simulations show linear destabilization of the VDOM by energetic particles. The linear modes are identified as VDOM by their mode structure and oscillation frequency of 184 kHz, in agreement with the observations of [11]. The bump-on-tail distribution provides an accessible 'knob,' the velocity shift $v_{\rm shift}$, for numeric scanning with an easy physical interpretation.

Figure 14 shows a plot of the linear growth as function of $V_{\rm shift}/V_{\rm therm}$. The scan shows that to excite the VDOM a minimum shift ($V_{\rm shift}/V_{\rm therm}\sim 1.2$) is necessary to bring the distribution into resonance and to overcome the damping of the background plasma. As $V_{\rm shift}$ increases, a maximum growth rate occurs when the VDOM resonance (at $\omega =$ 184 kHz) aligns with the maximum gradient, $\partial F_h/\partial v\backslash_{\mu={\rm const}}$, of the shifted bump-on-tail velocity distribution. The growth rate decreases as the bump-on-tail moves away from the VDOM resonance. Figure 15 shows the component of the plasma flow velocity, V_n; the $m = 1$ up-down parity in this contour plot is indicative of the VDOM. Also, the fast particle density, n_h, shown in figure 16, exhibits an $m = 1$ structure in the core but shifted in poloidal phase with respect to V_n. The $m = 1$ core is accompanied by an $m = 2$ structure towards the edge. Note

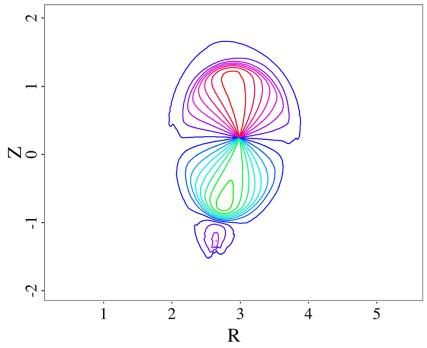

Figure 15. Contours of the normal component of the plasma flow velocity.

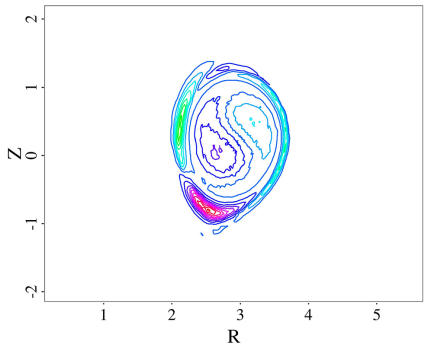

Figure 16. Contours of the fast particle density, n_h.

that these contours are snapshots in time and evolve over the VDOM period.

Simulations with more realistic distribution functions are underway and a more complete study will be reported in a subsequent publication.

8. Conclusions

In this article, an overview on the present state-of-the-art on $n = 0$ VDOM has been presented. These modes, as well as GAE, can provide a possible interpretation of experimental observations of n =0 modes observed in recent tokamak experiments, in particular, JET [6–8], TCV [9] and MAST-U [10].

The physical aspects that characterize VDOM and make them distinct from GAE are discussed in this article. The GAE can be defined as a shear-Alfvén internal mode, thus the main restoring force giving rise to plasma oscillations is related to field line bending. The GAE avoids continuum damping due to a minimum in the $k_{||}v_{\rm A}$ spectrum, so that its frequency lies just below the minimum value of $k_{||}v_{\rm A}$ reached inside the plasma. Consequently, the GAE mode structure tends to exhibit a rapid variation near the plasma edge, where the minimum of $k_{||}v_{\rm A}$ is found, because the safety factor q and the plasma density tend to vary quickly in that region. Thus, the GAE is sensitive to details of q and of plasma density, while its frequency, being an internal mode, is largely insensitive to the plasma-wall distance [15]. By contrast, the VDOM is an external mode. The main restoring force giving rise to oscillations is related to the interaction between the plasma current and

currents induced on the nearby first wall, under conditions of passive wall stabilization of the ideal-MHD vertical instability. The resulting electromagnetic force, coupling the plasma current and the induced wall currents, opposes further vertical movements (in the limit of a perfectly conducting wall), causing a global vertical oscillation of the entire plasma column [2]. Both VDOM and GAE are slightly damped by wall resistivity but can be driven unstable by resonant interaction with energetic particles in a tokamak plasma.

The main original results reported in this article are listed in the following:

(i) A discussion (section 3) on the limits of plasma elongation for stable operation against the vertical instability in the ideal-MHD limit. It is shown that, albeit in principle the critical elongation beyond which ideally unstable VDs become uncontrollable can be very large if the wall is very close and fits very tightly the plasma boundary, in practice a finite critical elongation always exists. An evaluation of the critical elongation for an idealized tokamak equilibrium and wall geometry is presented in section 3. An intriguing aspect is that, for elliptical and confocal plasma boundary and wall, and for a double-null configuration, the critical elongation corresponds to the situation where the wall intercepts the magnetic X-points. Ideal instability occurs when the X-points of this idealized equilibrium lie inside the vacuum chamber. However, these analytic considerations do not account for the possible presence on internal coils providing passive stabilization of vertical plasma displacements. Furthermore, for more realistic wall and plasma shaping configurations and for single-null divertor configurations, numerical work is required to assess stability thresholds in a more accurate manner.

(ii) An analytic study of VDOM in a straight tokamak configuration in the circular cross section limit is presented in section 4. The circular limit is useful in that in can clarify conditions for which VDOM may be affected by continuum damping. Typically, continuum damping happens when the density remains relatively large in the proximity of the plasma edge and the wall is very close to the plasma boundary, since the mode frequency increases as the wall-plasma distance decreases and, at some critical plasma-wall distance, it may become larger than the minimum value of $k_{||}v_{\rm A}$. This circumstance is more likely to occur when the equilibrium plasma density profile is H-mode-like, i.e. it exhibits a pedestal region near the plasma edge where the density drops rapidly to zero. By contrast, for L-mode-like density profiles, the VDOM is normally found to be immune of continuum damping.

(iii) The contributions to the drive of $n = 0$ modes by energetic ions have been studied in a semi-analytic way for two types of distribution functions associated with auxiliary heating: neutral beam injected ions and ions accelerated by ICRF waves. The energetic ion distribution functions for these cases at high energy are characterized by being rather narrow in the $\Lambda = \mu B_0/\varepsilon$ direction of phase space. As a result, there are both positive and negative contributions to the drive of the modes. The key question is therefore if the wave-particle interaction in the Λ region that contributes positively to the drive is more effective than the one giving a negative contribution. In the case of NBI, one finds that for a narrow distribution in Λ direction, there is a positive contribution to the drive if Λ_0 is greater than about 0.4 but below the Λ value corresponding to the trapped-passing boundary. A positive drive for ICRF heated ions has only been found if the resonance layer, where $\omega = n_{Ic}\omega_{ci}$ (the almost vertical layer where the wave frequency matches the cyclotron harmonic, n_{Ic}, of the interaction), is located on the high field side of the tokamak. In both cases the results were found to depend rather sensitively on the width of the distribution in the Λ direction, suggesting that for a credible assessment of the drive of $n = 0$ modes, modelling of the energetic ion distribution functions must be carried out with a high degree of physics fidelity.

(iv) New advances on the numerical simulation of $n = 0$ modes in realistic tokamak geometry using an initial-value code (NIMROD) are reported, with preliminary results showing VDOM driven by fast ions using a newly adapted kinetic-MHD module in NIMROD (section 7).

A discrepancy in the expression for the geometrical wall parameter D as reported by Wesson in [24, 31] in comparison with the corresponding expression obtained in [2, 3] and presented in this article is pointed out. A possible reason for this discrepancy is discussed in the appendix.

In section 5, we have pointed out that $n = 0$ modes treated within the framework of ideal-MHD are singular at the magnetic X-points of the divertor separatrix. Resolving the singularity by consideration of resistive effects reveals the formation of current sheets localized near the X-points and extending along the magnetic separatrix. The impact of these current sheets on the stability and turbulent behaviour of the plasma edge, and more in general, a study of 3D magnetic turbulence at the plasma edge in the presence of saturated $n = 0$ mode structures and zonal flows, is a natural continuation of this line of research.

Acknowledgments

We would like to thank JET collaborators, and in particular S. Sharapov, J. Oliver and M. Fitzgerald (UKAEA), for providing information and equilibrium reconstruction of interesting JET discharges where n=0 modes have been observed. We also acknowledge useful discussions with L. Villard (EPFL), M. Podestà (EPFL), M. Dreval (KIPT), and a stimulating discussion with Professor J. Freidberg (MIT) that led to the writing of section 3. We also thank Professor Huishan Cai and colleagues at the University of Science and Technology China at Hefei, where part of this work was carried out, for their kind hospitality. In particular, FP's stay at USTC was supported by USTC International Visiting Professor Grant No. 2025AVR04. SC's PhD grant was supported in part by E.N.I. S.p.A. NIMROD simulations were carried out using the HPC of the EUROFusion cluster.

Appendix. The geometrical wall parameter *D*

In this appendix, we address the question of the discrepancy between the expression for the geometric wall parameter D as given in equation (5), and the corresponding expression appearing in Wesson's article [24] as well as in section 6.15 of his well-known textbook 'Tokamaks' [31]. This discrepancy was also noted in [23].

To address this discrepancy, we consider the following publications: Laval *et al* [22], the already mentioned article by Wesson [24], and the articles by Barberis *et al* [2] and by Yolbarsop *et al* [3], where two independent derivations of equation (5) were provided. These publications are all concerned with the stability of VDs starting from a straight-tokamak equilibrium where the plasma current density is uniform, the cross-section of the plasma boundary is an ellipse with minor semi-axis a and major semi-axis b, and the cross-section of the wall is a confocal ellipse with minor semi-axis $a_{\rm w}$ and major semi-axis $b_{\rm w}$. Confocality means that ${b_{\rm w}}^2-{a_{\rm w}}^2=b^2-a^2$. The starting equilibrium is that worked out in [20, 21]. Since all these calculations are based on the same equilibrium assumptions, one should expect complete agreement between Laval *et al*, Wesson, and equation (5) appearing in this article. Unfortunately, as we shall see, while Wesson and equation (5) are both in agreement with Laval *et al*, they do not agree with each other. Wesson's work and the work leading to equation (5) both go one step further than Laval *et al*, and it is in this additional step where the disagreement is found.

Laval *et al* [22] present (among other things) an ideal-MHD stability analysis of axisymmetric VDs based on the energy principle, assuming a perfectly conducting wall. Thus, the parameter D does not appear in that article, but the marginal stability condition is explicitly worked out. In order to make contact with [22], we introduce the elliptical coordinate system (μ,ϑ):

$$x=A\,\sinh\mu\,\cos\vartheta;y=A\,\cosh\mu\sin\vartheta \tag{A.1}$$

where $A=\sqrt{b^2-a^2}$. Surfaces with constant-μ are confocal ellipses. The elliptical plasma boundary is labelled by $\mu=\mu_b$, such that $a=A\sinh\mu_b$ and $b=A\cosh\mu_b$. The confocal wall is labelled by , such that $a_w=A\sinh\mu_{\rm w}$ and $b_w=A\cosh\mu_{\rm w}$. Clearly, $\mu_{\rm w}\geqslant\mu_b$. Laval *et al* also introduce two parameters:

$$\begin{aligned}\alpha&=\exp\left(\mu_b-\mu_{\rm w}\right)=\frac{a+b}{a_{\rm w}+b_{\rm w}}\text{and}\\ \varepsilon&=\exp\left(-2\mu_b\right)=\frac{b-a}{b+a}.\end{aligned} \tag{A.2}$$

The most unstable modes are those with elliptical angle mode number $m=1$ (this has been tacitly assumed in our article). The marginal stability condition for axisymmetric $m=1$ modes as given in Laval *et al* [22] is written as

$$\alpha^2=\varepsilon,\text{or equivalently}\mu_{\rm w}=2\mu_b. \tag{A.3}$$

Now, let us turn to Wesson's article [24]. In section 2.3.1 of that article, he claims agreement with Laval *et al's* work [22] as far as the marginal stability condition for ideal-MHD VDs is concerned. The further step mentioned above is made in section 2.3.4, where axisymmetric modes with a resistive wall are considered. There, a cubic dispersion relation is presented *without derivation*. A parameter D appears, which can be written as

$$\begin{aligned}D&=D_{\rm W}-1\text{ where }D_{\rm W}=\frac{\alpha^2}{\varepsilon}\\ &=\left(\frac{b+a}{b-a}\right)\left(\frac{a+b}{a_{\rm w}+b_{\rm w}}\right)^2.\end{aligned} \tag{A.4}$$

In Wesson's notations, ideal-MHD marginal stability corresponds to $D=0$, or $D_W=1$. Therefore, as we can see, Wesson's expression for D agrees with the ideal-MHD marginal stability condition by Laval *et al*.

Wesson's parameter D differs from the one given in equation (5) in two different ways. One is very trivial: To avoid confusion, in this appendix we rename the parameter D appearing in equation (5) as D_{BYP} (from the initials of the three authors of [2]), then Wesson's D should correspond to $D_{\rm BYP}-1$. The crucial difference lies in the fact that $D_W\neq D_{BYP}$. To highlight this difference, we rewrite D_{BYP} as

$$D_{\rm BYP}=\frac{a^2}{\varepsilon}\frac{1+\exp\left(-4\mu_b\right)}{1+\exp\left(-2\mu_{\rm w}\right)}=\frac{\kappa^2+1}{\left(\kappa-1\right)^2}\frac{\kappa_{\rm w}-1}{\kappa_{\rm w}}. \tag{A.5}$$

As one can see, D_W and D_{BYP} are both equal to unity at ideal-MHD marginal stability, $\mu_{\rm w}=2\mu_b$, and so they both agree with the marginal stability criterion of Laval *et al* [22]. However, D_W and D_{BYP} are different away from ideal-MHD marginal stability.

The reason for this discrepancy is not completely clear. We point out that equation (5) was derived in two independent ways in [2] and in [3]. One can follow the derivation in the latter two references and, as far as we can tell, no errors can be spotted. Furthermore, the validity of the expression in equation (5), or its equivalent in equation (4), have been confirmed by numerical simulations using the extended-MHD code NIMROD, see [32, 34]. On the other hand, Wesson's derivation of equation (A.4) cannot be found in the published literature. Based on all these considerations, we are led to presume that the latter expression, Equation (A.4), is missing the factor multiplying α^2/ε in equation (A.5).

Regarding the equivalence between the two expressions for $D_{\rm BYP}$ in equations (4) and (5), we point out that, because of the confocality condition, the parameter D_{BYP} depends on two independent parameters that can be chosen to be, for instance, $\kappa=b/a$ and $\kappa_{\rm w}=b_{\rm w}/a_{\rm w}$, with $\kappa_{\rm w}\leqslant\kappa$, or alternatively κ and $b/b_{\rm w}$, where the parameter $b/b_{\rm w}\leqslant1$ measures the distance

between the wall and the plasma boundary along the vertical axis. One can go from equation (5) to (4) using

$$\frac{a_w}{b_w} = \sqrt{1 - \frac{\kappa^2 - 1}{\kappa^2}\left(\frac{b}{b_w}\right)} \tag{A.6}$$

which follows the confocality condition. Therefore, following also the discussion in [23], in order to avoid inconsistent results, one should keep in mind that a choice of the two parameters κ and κ_w automatically implies a specific value of b/b_w. For example, if one chooses $\kappa = 2$ and $\kappa_w = 1.5$, then equation (A.6) yields the value $b/b_w \approx 0.86$.

We remark, once more, that the assumptions on plasma-wall geometry and idealized equilibrium profiles described in sections 2, 3 and 4 are formulated to make the problem analytically tractable. The analytic solution is important in that it elucidates the mechanisms and structures underlying the $n = 0$ modes of interest and provide a benchmark for numerical simulations. However, these analytic solutions can at most suggest a qualitative interpretation of the $n = 0$ oscillations observed in tokamak experiments. For a more detailed comparison with experiments, numerical work becomes necessary, see e.g. [11]. In section 7 of the present article a discussion of how VDOMs are recognized in numerical simulations with realistic tokamak geometry and plasma equilibrium profiles is presented. Having said that, in some cases (especially when triangular shaping is not very strong) the wall cross-section in actual tokamak experiments may be shown to be contained between two ellipses that are confocal to an ellipse approximating the last closed flux surface. For these cases, the analytic results presented here may provide upper and lower bounds for the ideal-MHD stability of VDs, as well as, for the stable cases, an interval of possible values for the VDOM oscillation frequency.

ORCID iDs

F. Porcelli 0000-0002-3625-6417
D. Banerjee 0000-0002-7882-6369
T. Barberis 0000-0002-1030-7642
A. Yolbarsop 0000-0001-7686-0742

References

[1] Barberis T., Porcelli F. and Yolbarsop A. 2022 Fast-ion-driven vertical modes in magnetically confined toroidal plasmas *Nucl. Fusion* **62** 064002
[2] Barberis T., Yolbarsop A. and Porcelli F. 2022 Vertical displacement oscillatory modes in tokamak plasmas *J. Plasma Phys.* **88** 905880511
[3] Yolbarsop A., Porcelli F., Liu W. and Fitzpatrick R. 2022 Analytic theory of ideal-MHD vertical displacements in tokamak plasmas *Plasma Phys. Control. Fusion.* **64** 105002
[4] Porcelli F., Barberis T. and Yolbarsop A. 2023 Vertical displacements close to ideal-MHD marginal stability in tokamak plasmas *Fundam. Plasma Phys.* **5** 100017
[5] Oliver H.J.C., Sharapov S.E., Breizman B.N. and Zheng L.J. 2017 Axisymmetric global Alfvén eigenmodes within the ellipticity-induced frequency gap in the Joint European Torus *Phys. Plasmas* **24** 122505
[6] Kiptily V.G. *et al* 2021 Evidence for Alfvén eigenmodes driven by alpha particles in D-3He fusion experiments on JET *Nucl. Fusion* **61** 114006
[7] Oliver H.J.C. *et al* 2026 Axisymmetric eigenmodes excited by alpha particle energy gradients in JET D-T plasmas *Phys. Rev. Lett.* **136** 055101
[8] Sharapov S. *et al*, 2025 Fusion Alpha-Particle-Driven Alfvén Eigenmodes in JET D-T Plasmas: experiments and Theory *2025 IAEA Fusion Energy Conf.* (*Chengdu, 13–18 October 2025*)
[9] Dreval M., Sharapov S.E., Oliver H.J.C., Fitzgerald M., Karpushov A.N., Jansen van Vuuren A., Poley J., Podesta M. and Porcelli F. (the TCV Team and the EUROfusion Tokamak Exploitation Team) 2026 Axisymmetric global Alfvén eigenmodes in the TCV tokamak *Nucl. Fusion* **66** 086025
[10] Dreval K.K., Podestà M. and Sharapov S. (UKAEA) 2025 Personal communication
[11] Barberis T., Kim C.C., Porcelli F., Banerjee D., Hawkes N., Kazakov Y.O., Liu Y.Q., Oliver H.J.C., Sharapov S. and Yolbarsop A. 2024 Simulations of vertical displacement oscillatory modes and global Alfvén Eigenmodes in JET geometry *Nucl. Fusion* **64** 126064
[12] Yolbarsop A., Porcelli F. and Fitzpatrick R. 2021 Impact of magnetic X-points on the vertical stability of tokamak plasmas *Nucl. Fusion* **61** 114003
[13] Porcelli F. *et al* 2025 n=0 vertical displacements, impact of magnetic X-points and vertical displacements oscillatory modes driven by fast ions in tokamak plasmas *2025 IAEA Fusion Energy Conf.* (*Chengdu, 13–8 October 2025*)
[14] Fu G.Y. 2008 Energetic-particle-induced geodesic acoustic mode *Phys. Rev. Lett.* **101** 185002
[15] Villard L. and Vaclavik J. 1997 Alfvén frequency modes and global Alfvén eigenmodes *Nucl. Fusion* **37** 351–60
[16] Fitzpatrick R. 2009 A simple ideal magnetohydrodynamical model of vertical disruption events in tokamaks *Phys. Plasmas* **16** 012506
[17] Strait E.J., Lao L.L., Luxon J.L. and Reis E.E. 1991 Observation of poloidal current flow to the vacuum vessel wall during vertical instabilities in the DIII-D tokamak *Nucl. Fusion* **31** 527–34
[18] Granetz R.S., Hutchinson I.H., Sorci J., Irby J.H., LaBombard B. and Gwinn D. 1995 Disruptions and halo currents in Alcator C-Mod *Nucl. Fusion* **36** 545
[19] Albanese R., Mattei M. and Villone F. 2004 Prediction of the growth rates of VDEs in JET *Nucl. Fusion* **44** 999–1007
[20] Porcelli F. and Yolbarsop A. 2019 Analytic equilibrium of "straight tokamak" plasma bounded by a magnetic separatrix *Phys. Plasmas* **26** 054501
[21] Gajewski R. 1972 Magnetohydrodynamic equilibrium of an elliptical plasma cylinder *Phys. Fluids* **15** 70–74
[22] Laval G., Pellat R. and Soule J.S. 1974 Hydromagnetic stability of a current-carrying pinch with noncircular cross section *Phys. Fluids* **17** 835–45
[23] Chukashev N.V. and Pustovitov V.D. 2025 Analytical estimates of the vertical displacement growth rate in tokamaks with a resistive wall *Phys. Plasmas* **32** 032511
[24] Wesson J.A. 1978 Hydromagnetic stability of tokamaks *Nucl. Fusion* **18** 87–132
[25] Villone F. and Pustovitov V.D. 2013 Skin effect modifications of the resistive wall mode dynamics in tokamaks *Phys. Lett. A.* **377** 2780–4
[26] Yanovskiy V. 2016 Theoretical analysis of tokamak disruptions by simplified analytical models and numerical simulations *(University degli Studi di Padova)*
[27] Jardin S.C. and Larrabee D.A. 1982 Feedback stabilization of rigid axisymmetric modes in Tokamaks *Nucl. Fusion* **22** 1095–8

[28] Pfefferlé D. and Bhattacharjee A. 2018 Algebraic motion of vertically displacing plasmas *Phys. Plasmas* **25** 022516
[29] Olofsson K.E.J. 2022 Fast calculation of the tokamak vertical instability *Plasma Phys. Control. Fusion.* **64** 072001
[30] Fukuyama A., Seki S., Momota H. and Itatani R. 1975 Positional instabilities in a Tokamak with a resistive shell *Jpn. J. Appl. Phys.* **14** 871–8
[31] Wesson J.A. 2011 *Tokamaks* 4th edn (Oxford University Press)
[32] Yolbarsop A., Porcelli F., Banerjee D., Kim C.C. and Hong L. 2023 Axisymmetric oscillatory modes in cylindrical magnetized plasma bounded by a conducting wall, physics letters, section a: general *Phys. Lett. A.* **479** 128940
[33] Strauss H.R. 1976 Nonlinear, three-dimensional magnetohydrodynamics of noncircular tokamaks *Phys. Fluids* **19** 134–40
[34] Banerjee D., Kim C.C., Barberis T. and Porcelli F. 2024 Linear NIMROD simulations of n = 0 modes for straight tokamak configuration and comparison with analytic results *Phys. Plasmas* **31** 023904
[35] Lingertat J. *et al* 1997 Studies of giant ELM interaction with the divertor target in JET *J. Nucl. Mater.* **241** 402–7
[36] Solano E.R. *et al* 2016 Axisymmetric oscillations at L–H transitions in JET: m-mode *Nucl. Fusion* **57** 022021
[37] Krebs I., Artola F.J., Sovinec C.R., Jardin S.C., Bunkers K.J., Hoelzl M. and Ferraro N.M. 2020 Axisymmetric simulations of vertical displacement events in tokamaks: a benchmark of M3D-C1 *NIMROD, and JOREK Phys. Plasmas* **27** 022505
[38] Porcelli F., Stankiewicz R., Kerner W. and Berk H.L. 1994 Solution of the drift-kinetic equation for global plasma modes and finite particle orbit widths *Phys. Plasmas* **1** 470–80
[39] Barberis T. and Porcelli F. 2024 Velocity-space distribution function of fast ions in a saw toothing plasma *Plasma Phys. Control. Fusion.* **66** 075007
[40] Van Zeeland M.A. *et al* 2021 Beam modulation and bump-on-tail effects on Alfvén eigenmode stability in DIII-D *Nucl. Fusion* **61** 066028
[41] Eriksson L.-G. and Porcelli F. 2025 On the drive of n_φ = 0 modes by ICRF accelerated ions in a tokamak *Nucl. Fusion* **65** 092005
[42] Sovinec C.R., Glasser A.H., Gianakon T.A., Barnes D.C., Nebel R.A., Kruger S.E., Schnack D.D., Plimpton S.J., Tarditi A. and Chu M.S. 2004 Nonlinear magnetohydrodynamics simulation using high-order finite elements *J. Comput. Phys.* **195** 355–86
[43] Kim C.C. (the NIMROD Team) 2008 Impact of velocity space distribution on hybrid kinetic-MHD simulation of the (1,1) mode *Phys. Plasmas* **15** 072507